International Journal of Fracture **79**: 309–340, 1996.

A transferability model for brittle fracture including constraint and ductile tearing effects: a probabilistic approach

CLAUDIO RUGGIERI and ROBERT H. DODDS, Jr.
Department of Civil Engineering, University of Illinois, Urbana, IL 61801, USA

Received 30 October 1995; accepted in revised form 4 June 1996

Abstract. This study describes a computational framework to quantify the influence of constraint loss and ductile tearing on the cleavage fracture process, as reflected by the pronounced effects on macroscopic toughness (J_c, δ_c). Our approach adopts the Weibull stress σ_w as a suitable near-tip parameter to describe the coupling of remote loading with a micromechanics model incorporating the statistics of microcracks (weakest link philosophy). Unstable crack propagation (cleavage) occurs at a critical value of σ_w which may be attained prior to, or following, some amount of stable, ductile crack extension. A central feature of our framework focuses on the realistic numerical modeling of ductile crack growth using the computational cell methodology to define the evolution of near-tip stress fields during crack extension. Under increased remote loading (J), development of the Weibull stress reflects the potentially strong variations of near-tip stress fields due to the interacting effects of constraint loss and ductile crack extension. Computational results are discussed for well-contained plasticity, where the near-tip fields for a stationary and a growing crack are generated with a modified boundary layer (MBL) formulation (in the form of different levels of applied T-stress). These analyses demonstrate clearly the dependence of σ_w on crack-tip stress triaxiality and crack growth. The paper concludes with an application of the micromechanics model to predict the measured geometry and ductile tearing effects on the cleavage fracture toughness J_c of an HSLA steel. Here, we employ the concept of the Dodds–Anderson scaling model, but replace their original local criterion based on the equivalence of near-tip stressed volumes by attainment of a critical value of the Weibull stress. For this application, the proposed approach successfully predicts the combined effects of loss of constraint and crack growth on measured J_c-values.

1. Introduction

Conventional assessments of elastic-plastic fracture behavior in large engineering structures using laboratory specimen data employ a one-parameter characterization of loading and toughness, most commonly the J-integral or the corresponding value of the Crack Tip Opening Displacement (CTOD, δ). The approach correlates unstable crack propagation in different cracked bodies based on the similarity of their respective near-tip stress and strain fields (see, e.g., the review by Hutchinson [1]). However, the deficiencies of such a one-parameter idealization become increasingly clear by examining the evolution of crack-tip fields for different ranges of near-tip constraint induced by shallow crack configurations and/or remote tensile loading. The early numerical analyses of McMeeking and Parks [2], and Shih and German [3] demonstrated the strong dependence of crack-tip fields on specimen geometry and remote loading, particularly for moderate-to-low hardening materials under large scale yielding conditions. Subsequent experimental studies, see [4, 5, 6] for illustrative data, have also shown significant elevations (factors exceeding 3–5) in the elastic-plastic fracture toughness for shallow crack SE(B) specimens of ferritic steels tested in the transition region, where transgranular cleavage triggers macroscopic fracture. The enormous practical implications of this *apparent* increased toughness of common ferritic steels in low-constraint conditions, particularly in defect assessment – repair decisions of in-service structures, have spurred a flurry of new analytical, computational and experimental research over the past five years.

In the spirit of extending 'correlative' fracture mechanics, researchers have developed more realistic descriptions of crack-tip stress and deformation fields which explicitly address the varying near-tip constraint prior to any ductile crack extension. In particular, approaches based on a two-parameter characterization of crack-tip fields, such as the T-stress [7–11] and the nondimensional Q-stress [12, 13], construct families of mode I, elastic-plastic crack-tip fields having different levels of near-tip stress triaxiality. In both approaches, J sets the magnitude of near-tip deformation (CTOD), while the second parameter characterizes the associated level of stress triaxiality over distances comparable to a few CTODs. The J-T and J-Q approaches remain essentially equivalent under small-scale yielding conditions, whereas the Q-parameter seems more appropriate for fully-yielded conditions (as the elastic conditions upon which the T-stress rests become increasingly violated). Nevertheless, both approaches may be employed in laboratory testing programs to generate material toughness loci applicable in the lower-transition region where significant plasticity occurs without prior ductile tearing at fracture.

Two-parameter approaches retain contact with traditional fracture mechanics and provide a concise framework to represent measured toughness values in terms of a J-T or J-Q locus. However, they do not provide a means to *predict* the effects of constraint variations and prior ductile tearing on toughness. Such predictions necessarily require a more detailed description of the fracture process, and are most often accomplished through recourse to micromechanics models that employ *local* fracture criteria (collectively referred to as *local approaches*). Local approaches couple the (stress-strain) loading history in the near-tip region where fracture takes place with the (operative) microstructural fracture mechanism. A fracture parameter reflecting local *damage* of material near the crack tip reaches a critical value at material failure. Overall fracture conditions in a specimen or structural component may then be described by evolution of the micromechanistically based parameter with the macroscopic loading, defined conveniently by J or CTOD. In particular, micromechanics models that employ the statistics of microcracks provide an approximate treatment of observed phenomena associated with cleavage fracture, specifically the large scatter in fracture toughness data in the transition range.

Several approaches along these lines have been proposed to relate local failure conditions with macroscopic fracture parameters and to the subsequent prediction of toughness loci. For the transgranular cleavage mechanism of ferritic steels, a number of such models explicitly adopt weakest link arguments that yield statistical functions reflecting the inhomogeneous character of near-tip stresses [14–17]. Work of the Beremin group [17] attains particular relevance here as it introduced the so-called Weibull stress as a local fracture parameter. Similar statistical approaches falling within the scope of micromechanics methodologies have also been described by Wallin et al. [18, 19, 20], Lin et al. [21], Mudry [22], Brückner et al. [23, 24], Minami et al. [25], Bakker et al. [26, 27], Ruggieri et al. [28], among others. Dodds and Anderson [29, 30] have proposed to quantify the *relative* effects of constraint variations on cleavage fracture toughness in the form of a *toughness scaling model*. They approached loss of crack-tip constraint by postulating the material volume ahead of the crack front over which the principal stress exceeds a critical value as the local fracture criterion. The toughness scaling model provides the ratio of J-values across different specimens which generate equal stressed volumes. While their model makes no explicit recourse to a statistical function, it shares the essential underlying features of the previously noted micromechanics (statistical) approaches.

In the mid-to-upper transition region, a strong competition develops between cleavage and ductile tearing mechanisms of crack extension. For materials having sufficient resistance to cleavage fracture at the higher temperatures, intense plastic strains coupled with high stresses directly ahead of the blunting crack tip generally produce ductile tearing prior to unstable crack propagation by cleavage (ductile tearing up to 5 mm has been observed). Ductile extension of the crack front alters the stress histories (relative to a stationary crack) in material ahead of the blunting region and increases the volume of the fracture process zone [31, 32]. The inclusion of ductile crack growth effects on the local stress-strain fields that drive micromechanics models for cleavage fracture becomes central to quantifying constraint effects in mid-to-upper transition.

This study describes a methodology, based on a local failure model employing the statistics of microcracks, to predict the strongly interacting effects of ductile tearing and constraint variations on (macroscopic) cleavage fracture toughness. We limit our focus to a stress-controlled, cleavage mechanism for material failure and adopt the Weibull stress (σ_w) as the local parameter to describe crack-tip conditions. Unstable crack propagation occurs at a critical value of σ_w which may be attained prior to or following some amount of stable, ductile crack extension; the outcome being determined by the specimen geometry, mode of loading (tension or bending), material flow properties and micro-scale tearing resistance. Here, the critical Weibull stress represents a property of the material, possibly dependent on temperature, but invariant of loading history. When implemented in a finite element code, the computational model predicts the evolution of Weibull stress with applied J while the crack tip undergoes first blunting and then stable, ductile crack extension.

To incorporate ductile crack growth, we utilize the *computational cell* model proposed by Xia and Shih [33–35]. A simplified form of the Gurson–Tvergaard (GT) constitutive model [37, 38] for dilatant plasticity predicts microscopic void growth within a layer of elements (cells) of height $\approx \delta_{1c}$ defined over the remaining ligament. The cell size defines a length-scale over which damage occurs and enters the model as an explicitly specified parameter. Outside of this layer, the material follows a conventional J_2 flow theory, possibly undergoing finite strains. Crack extension over a cell occurs when the initial void (volume) fraction increases to a critical value; an extinction procedure then deletes the cell. We calibrate the initial/final void fraction of the GT model and the cell size from known experimental $J - \Delta a$ curves for the material constructed from the measured critical J values and crack extensions of specimens that failed by cleavage after various amounts of crack growth. Although the computations reported here are carried out in a (finite deformation) plane-strain framework, reference is made to on-going work which addresses the general case of 3-D crack configurations.

Computational results are reported first for stationary and growing cracks in well-contained plasticity, where the near-tip fields of varying constraint are generated through a modified boundary layer (MBL) formulation (in the form of different values of applied T-stress). Although these solutions lack a rigorous correspondence with fracture specimens under fully-yielded conditions, they represent a wide class of cleavage failure modes exhibiting severe loss of constraint and small amounts of ductile tearing. The numerical results focus on an application of the micromechanics model to predict specimen geometry and stable crack growth effects on the macroscopic fracture toughness (J_c) of a high-strength, low alloy (HSLA) steel. We express the analysis results in terms of a modified Dodds–Anderson toughness scaling model. Their original local criterion based on the equivalence of near-tip stressed volumes is replaced by the attainment of a critical Weibull stress. The scaling model curves then expresses ratios of critical J-values for differing constraint levels and amounts of stable crack extension

which generate the same Weibull stress. Measured deep-notch toughness values, without crack growth, enable calibration of the Weibull modulus for the material. The GT model parameters and cell size are calibrated using an R-curve constructed from shallow-notch tests. Details of both calibration procedures are provided. For this material, the proposed methodology successfully predicts the measured statistical distribution of cleavage fracture toughness in shallow crack specimens, reflecting the combined effects of constraint loss and crack growth.

2. Statistical treatment of cleavage fracture

The initiation of transgranular cleavage fracture in ferritic steels occurs primarily by the formation of microcracks at carbides, most often dispersed along grain boundaries, in regions which undergo locally inhomogeneous plastic flow; these cracked carbides provide the cleavage nucleation sites [39]. A qualitative description of cleavage fracture, consistent with these early experimental observations, identifies the critical event for unstable propagation of a macroscopic crack as the growth of microcracks upon reaching certain critical conditions. Here, we adopt the viewpoint that unstable crack propagation occurs when the local tensile stress within a fracture process zone ahead of a crack or a notch reaches a critical tensile stress σ_c [40].

The random nature of cleavage fracture due to inhomogeneity in the local characteristics of the material drives the development of a relationship to couple macroscopic fracture behavior with microscale events. Consequently, we consider a micromechanics model that employs the statistics of microcracks applicable for ferritic steels in the transition region. A connection between the microcracking process, a continuum view of the material and a tractable mathematical formulation follows by assuming a random distribution of flaws; their size and density constitute properties of the material. Further, there exists small, but finite, volumes of material which fully embody a population of uniformly distributed flaws. Statistical considerations therefore reduce the brittle fracture problem to one of finding a critical flaw or, in general, of determining the extreme value distribution of flaw size.

2.1. The Weibull stress for cracked solids

We begin by introducing a limiting distribution for the fracture stress of a cracked body subjected to a multiaxial stress state, where a *stationary* macroscopic crack lies in a material containing randomly oriented microcracks, uniformly distributed in location. The 3-D form is given first and then simplified to plane strain conditions appropriate for the present investigation. We idealize the fracture process zone near the crack tip as formed by a large number of statistically independent and uniformly stressed, small volume elements, denoted δV. Figure 1 illustrates a stressed region near a crack or a notch where an arbitrary volume V is subjected to a stress state σ. Based upon probability theory and invoking the Poisson postulates (see, e.g., Feller [41]), the elemental failure probability $\delta\mathcal{P}$ is related to the distribution of the largest flaw in a reference volume of the material, which can be expressed as

$$\delta\mathcal{P} = \delta V \int_{a_c}^{\infty} g(a)\,\mathrm{d}a, \tag{1}$$

where $g(a)\,\mathrm{d}a$ defines the average number of microcracks per unit volume having sizes between a and $a + \mathrm{d}a$. Here, a common assumption adopts an asymptotic distribution for the microcrack density in the form $g(a) = (1/V_0)(c_0/a)^c$, where c and c_0 are parameters of the

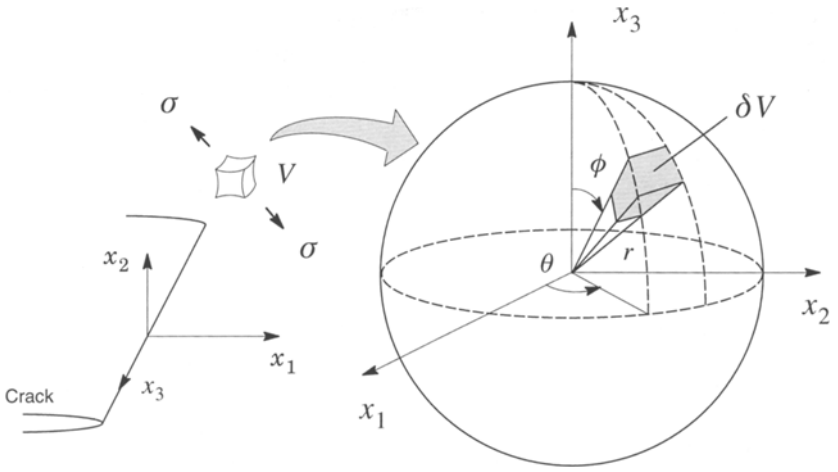

Figure 1. Stressed volume ahead of crack tip.

distribution and V_0 denotes a reference volume [42, 43]. The implicit distribution of fracture stress can be made explicit by introducing the dependence between the critical microcrack size a_c and stress in the form $a_c = (K^2/Y\sigma^2)$, where Y represents the specimen dependent geometry factor and σ denotes a tensile (opening) stress acting on the microcrack plane. A simple manipulation of this expression on the basis of weakest link statistics yields the limiting distribution for the fracture strength of a cracked solid in conventional spherical coordinates (r, θ, ϕ) as [45, 46]

$$\mathcal{P}(\sigma) = 1 - \exp\left[-\frac{1}{4\pi V_0}\int_\Omega \int_0^{2\pi} \int_0^{\pi} \left(\frac{\sigma}{\sigma_u}\right)^m \sin\phi \, \mathrm{d}\phi \, \mathrm{d}\theta \, \mathrm{d}\Omega\right], \tag{2}$$

where Ω denotes the volume of the (near-tip) fracture process zone, and parameter $m = 2c-2$ and σ_u define the microcrack distribution. Since the reference volume V_0 only scales $g(a)$ but does not change the distribution shape, it has no effect on m and is conveniently assigned a unit value in computations.

Equation (2) implicitly defines a zero threshold stress for fracture; consequently, stresses vanishingly small compared to the fracture stress yield a nonzero (albeit small) probability for fracture. A more refined form of the limiting distribution for the fracture strength of a cracked solid is given by

$$\mathcal{P}(\sigma) = 1 - \exp\left[-\frac{1}{4\pi V_0}\int_\Omega \int_0^{2\pi} \int_0^{\pi} \left(\frac{\sigma - \sigma_{\text{th}}}{\sigma_u}\right)^m \sin\phi \, \mathrm{d}\phi \, \mathrm{d}\theta \, \mathrm{d}\Omega\right], \quad \sigma \geqslant \sigma_{\text{th}}, \tag{3}$$

where σ_{th} denotes the threshold stress and has the physical interpretation of a lower-bound strength for fracture. The failure probability for the cracked solid becomes zero for any stress below σ_{th}. However, as will be demonstrated in Section 5, such refinement does not appear to provide significant improvements in the fracture behavior predicted by the present methodology. Debate over a physically meaningful value for σ_{th} continues. Subsequent equations remain valid for any $\sigma_{\text{th}} > 0$ upon substitution of $\sigma - \sigma_{\text{th}}$ for σ.

Following this general development, the Beremin's Weibull stress [17] is given by integration of the tensile stresses over the fracture process zone in the form

$$\sigma_w = \left[\frac{1}{4\pi V_0}\int_\Omega \int_0^{2\pi}\int_0^{\pi} \sigma^m \sin\phi \, \mathrm{d}\phi \, \mathrm{d}\theta \, \mathrm{d}\Omega\right]^{1/m} \tag{4}$$

from which the limiting distribution (2) now takes the form

$$\mathcal{P}(\sigma_w) = 1 - \exp\left[-\left(\frac{\sigma_w}{\sigma_u}\right)^m\right]. \tag{5}$$

Equation (5) defines a two-parameter Weibull distribution [44] in terms of the Weibull modulus m and the scale parameter σ_u. Previous work [6, 17, 25] has shown that m takes a value in the range $10 \sim 22$ for typical structural steels.

A similar formulation applies under plane strain conditions for which the fracture process zone ahead of the crack tip remains uniform along the crack front. A volume element $\mathrm{d}\Omega$ becomes simply $B\,\mathrm{d}A$, where B represents the thickness of the cracked body and $\mathrm{d}A$ lies within the process zone in the x_1–x_2 plane (see Fig. 1). The Weibull stress for plane-strain conditions then takes the form

$$\sigma_w = \left[\frac{B}{\pi V_0}\int_A \int_0^{\pi} \sigma^m \, \mathrm{d}\theta \, \mathrm{d}A\right]^{1/m}, \tag{6}$$

where B may be simply assigned a reference unit thickness as shown later.

2.2. Generalization of the Weibull Stress for a Growing Crack

The Weibull stress describes local conditions leading to unstable (cleavage) failure and appears, at least as a first approximation, to remain applicable during small amounts of ductile crack extension. However, the potential fracture process zone for an extending crack now comprises three distinct *zones* depending upon the material's stress history. Figure 2 provides a schematic illustration of the three zones, denoted as A, B, and C. Material in the unloaded zone A *behind* the current physical location of the advancing crack tip, but previously located *ahead* of the tip, experienced severe stress and strain fields without triggering cleavage fracture. Due to blunting at the location of the physical crack tip, the peak value of opening mode stress develops at a small distance (roughly the blunted opening) ahead of the tip. Material in the region between the crack tip and the peak stress location (zone B) experiences significant damage due to void growth with a corresponding stress reduction. Earlier in the loading history, this material (which still contains potential cleavage sites) was *ahead* of the peak stress location, and thus has experienced unloading in terms of the continuum stress field accompanied by a large increase in (tensile) plastic strain. Finally, material located outside the blunting region (zone C) experiences increased stresses with consequent generation of new microcracks and cracked carbides due to progressive plastic deformation.

The evolution of Weibull stress during crack growth obviously depends on the choice of the fracture process zone. Cleavage cracking in the unloaded region behind the crack tip (zone A) does not appear sufficient to trigger unstable propagation of the macroscopic crack. Furthermore, it seems not at all certain that material in zone A, which has previously suffered

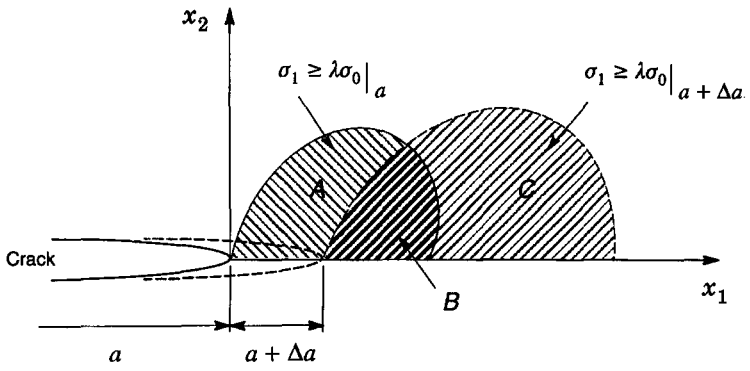

Figure 2. Evolution of the fracture process zone for a growing crack.

some damage due to growth, effectively contributes to the *current* failure probability of the cracked body.

In contrast, small amounts of ductile crack growth can modify the stress history of material *ahead* of the crack tip, especially in zone C, which affects strongly the propensity for unstable propagation of the macroscopic crack. For material in zones B and C, previous studies of ductile crack growth [31, 32] have revealed that:

(1) for geometries with low constraint prior to growth, stress triaxiality ahead of the crack tip increases significantly during growth due to elastic unloading behind and macroscopic re-sharpening of the advancing tip,
(2) for geometries with high constraint prior to growth, only minor elevations in peak stress triaxiality occur, and
(3) for all cases, the extent of the region of higher stress triaxiality increases leading to a larger process zone for cleavage fracture.

Thus, we propose to define the *active* fracture process zone, which moves forward with the advancing tip and increases in size, as the loci $\sigma_1 \geqslant \lambda\sigma_0$, encompassing zones B and C, with $\lambda \approx 2$. As illustrated in Figure 2, the development of such a region is given by a snapshot of the stress field ahead of the growing crack; points on such a contour all lie within the forward sector $|\theta| \leqslant \frac{1}{2}\pi$.

The present definition of the *active* process zone is motivated by considering the essential features of the micromechanism for cleavage fracture ahead of a macroscopic crack. In ferritic steels, cracked carbides formed in the course of plastic deformation provide the potential sites for nucleation of cleavage microcracks. Highly localized, non-planar crack extension and void growth at the larger inclusions, both of which occur over a scale roughly smaller than δ_{Ic} within zone B, should not alter the material properties m and σ_u over the much larger process zone relevant for cleavage initiation, zone C. Moreover, m values for structural steels in the 10–22 range severely reduce the contribution to σ_w made by the current opening mode stresses in zone B. Brückner-Foit et al. [23] have recently examined the distribution of locations for the origin of cleavage fracture in a pressure vessel steel; their fractographic results provide additional support for the active process zone proposed here.

The active process zone places a strong emphasis on the contribution of material points located in zone C, which are expected to trigger macroscopic crack propagation. When the macroscopic crack advances by ductile tearing at a loading level still insufficient to cause

brittle fracture in the specimen or structural component, material elements within the partially unloaded region near the crack tip (zone B) did not trigger cleavage fracture, but nonetheless sustain residual stresses and large plastic strains. The *survival* of these material elements implies that a critical condition has not been achieved, i.e., unstable propagation of the most severe microcrack did not take place. The contribution of these material elements in the total failure probability grows smaller as loading progresses. However, the *total* failure probability for the cracked solid monotonically *increases* with increased loading since crack growth elevates the near-tip stress triaxiality and enlarges the volume of material containing potential cleavage sites. Consequently, the 3-D form of the Weibull stress for a growing crack becomes simply

$$\sigma_w = \left[\frac{1}{4\pi V_0} \int_{\Omega^*} \int_0^{2\pi} \int_0^{\pi} \sigma^m \sin\phi \, \mathrm{d}\phi \, \mathrm{d}\theta \, \mathrm{d}\Omega^* \right]^{1/m}, \tag{7}$$

where Ω^* denotes the volume of the active fracture process zone, $\sigma_1 \geqslant \lambda\sigma_0$, which moves forward with the advancing tip. The plane-strain form of (7) is similar to (6) with the tensile stresses being integrated over the area A^* of the active process zone. The proposed generalization of σ_w to include ductile tearing maintains the relative simplicity of computations while, at the same time, fully incorporating the effects of alterations in the stress field ahead of the crack tip.

In related work to characterize cleavage fracture in the DBT transition region for ferritic steels, Bakker and co-workers [26, 27] also extend the Weibull stress concept to include damage of material located within the region where partial unloading occurs (zone B). However, they replace the *current* stress in (7) with the *maximum* stress that the material point has experienced during the entire loading history (generally the peak stress). Compared to the present proposal, their procedure may emphasize the contribution of material in zone B toward the total failure probability. Currently, we consider the correct treatment of local failure probability for material elements in zone B as unresolved. Section 5.2 addresses this issue and compares the evolution of σ_w with macroscopic loading (as characterized by J) using the present definition of the active process zone and the maximum stress approach; the results here reveal that both procedures are essentially equivalent for the material and specimens analyzed.

2.3. A MODIFIED TOUGHNESS SCALING MODEL

Dodds and Anderson (D-A) [29, 30] proposed a simplified micromechanics treatment to predict constraint effects on cleavage fracture toughness prior to ductile tearing. The procedure, usually referred to as the *toughness scaling model*, requires attainment of equivalent stressed volumes ahead of a crack front for cleavage fracture in different specimens, even though the J values may differ markedly. Without explicit reference to microstructural parameters that describe the distribution of cleavage microcracks, the D-A model predicts the variation of fracture toughness with constraint changes for a given material/temperature by scaling specimen toughness levels to a convenient reference constraint condition, most often SSY with $T \equiv 0$. The model enables robust predictions of constraint effects on cleavage fracture toughness provided the crack-tip stress fields of the various specimens differ only in the level of triaxiality [60], i.e., contours of principal stress change only in 'size' and not in 'shape' under increased specimen loading. In contrast, consider two specimens which have the same material volume within a specified principal stress contour $\sigma_1/\sigma_0 = \tilde{\sigma}_c$ but which have strongly

different radial and circumferential stress fields ahead of the crack tip. The D-A model does not reflect such variations, with equal weight attributed to all material volumes having $\sigma_1/\sigma_0 \geqslant \tilde{\sigma}_c$. Ductile crack extension generates near-tip stress fields sufficiently different in character from stationary near-tip fields to question the validity of D-A model predictions between the two conditions.

To overcome these limitations, the present work proposes a modified toughness scaling model to assess the combined effects of constraint variations and ductile tearing on cleavage fracture toughness data. Based upon micromechanics considerations outlined previously, the modified scaling model requires the attainment of a specified value for the Weibull stress to trigger cleavage fracture in different specimens even though J-values may differ widely. The procedure illustrated in Figure 3 aims to predict the fracture toughness *distribution* for configurations exhibiting low levels of crack-tip stress triaxiality, such as shallow notch SE(B) specimens, from the measured toughness values obtained using high constraint, deep notch specimens, SE(B) or C(T) specimens. The specimens may or may not experience stable ductile tearing; however, low constraint specimens typically exhibit larger amounts of stable tearing. Figure 3(a) shows the distribution of Weibull stress values for deep notch specimens (configuration A); solid symbols correspond to the Weibull stress at measured values of fracture toughness while the solid line represents the maximum likelihood fitting of these values. This distribution obeys the two-parameter Weibull model given by (5) where the parameters (m, σ_u) are calibrated using the procedure outlined in Section 5.2. Figure 3(b) presents curves of σ_w versus J (or equivalently CTOD) for the deep notch specimen and for the shallow notch SE(B) specimen. Finite element analyses provide the stress fields to evaluate σ_w for the specimens at a fixed, specified value of the Weibull modulus m. Section 3.6 describes the numerical procedures to compute σ_w. The Weibull modulus, m, represents a material property in the current model. It must be employed to generate the Weibull stress versus J curves for all specimens of the material at the temperature under consideration. Figure 3(c) shows the *predicted* probability distribution for the shallow notch SE(B) specimen (configuration B) indicated by the solid line.

The fitted distribution of σ_w-values for the deep notch specimens (configuration A) shown in Figure 3(a) provides the corresponding *distribution* of J_c-values for these specimens. These J_c-values are not the *actual* values measured in the experiments; they are generated from $\mathcal{P}_A(\sigma_w)$ using the calibrated values $(\hat{m}, \hat{\sigma}_u)$. This procedure enables construction of confidence bounds for the predicted distribution of the shallow notch specimens when the distribution of J_c-values is generated using the confidence bounds for the Weibull parameters. By employing the scaling model form of the Weibull stress curves illustrated in Figure 3(b), the generated, continuous function of J_c-values for the deep notch specimens (configuration A) is 'corrected' as shown for the effects of constraint loss and crack extension to *predict* the corresponding values for the shallow notch SE(B) specimens (configuration B). Note that each point on curve $\mathcal{P}_A(\sigma_w)$ correspondes to another point on curve $\mathcal{P}_B(J_c^B)$ with the same probability of fracture, i.e., $\mathcal{P}_A(\sigma_w) = \mathcal{P}_B(J_c^B)$. Therefore, the probability distribution of cleavage fracture toughness for configuration B can be expressed in closed form as

$$\mathcal{P}(J_c^B) = 1 - \exp\left[-\left(\frac{\mathrm{F}_B(J_c^B, m)}{\sigma_u}\right)^m\right], \tag{8}$$

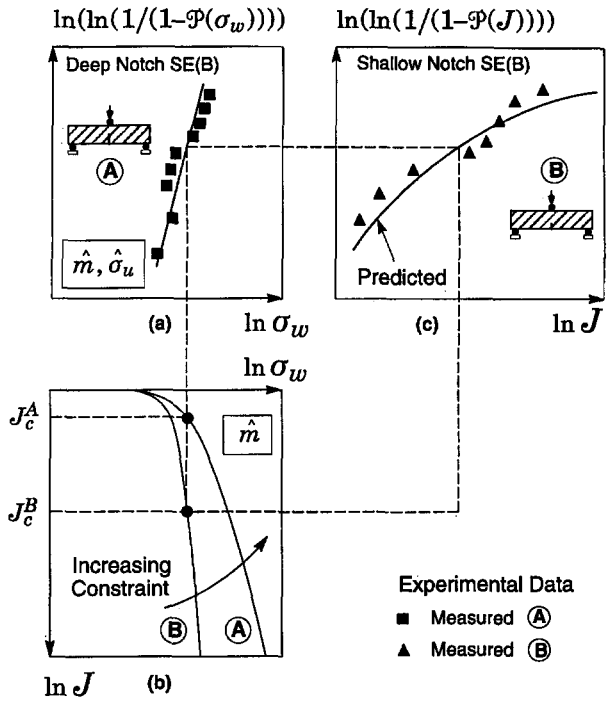

Figure 3. Scaling methodology employed to predict the probability distribution of fracture toughness data in different specimens or crack configurations.

where $\mathrm{F}_B(J, m)$ denotes the computed functional relationship between J (or equivalently CTOD) in configuration B (finite element model) and the Weibull stress for the calibrated value of m.

While this predictive methodology is similar to the original D-A procedure, a key enhancement arises when using the present failure criterion. The Weibull stress incorporates *both* the effects of stressed volume (as in the D-A model) and the potentially strong changes in the character of the near-tip stress fields due to constraint loss and ductile crack extension. The modified model clearly reflects a closer correspondence with the micromechanical features of the cleavage fracture process.

3. Computational procedures and geometric models

3.1. Ductile crack growth using computational cells

The *computational cell* methodology proposed by Xia and Shih [33–35] (X&S) provides a model for ductile crack extension that includes a realistic void growth mechanism, and a microstructural length-scale physically coupled to the size of the fracture process zone. This section provides a brief synopsis of the methodology relevant to the current study of mixed tearing and cleavage mechanisms. Figure 4(a) depicts a crack tip growing under mode I conditions into material which contains two, uniformly distributed populations of large and small inclusions. The larger inclusions (e.g., MnS) provide sites for the formation of microstructural voids which grow, then coalesce with the current crack tip to create new crack surfaces. The smaller inclusions (e.g. carbides) provide initiation sites for sharp microcracks

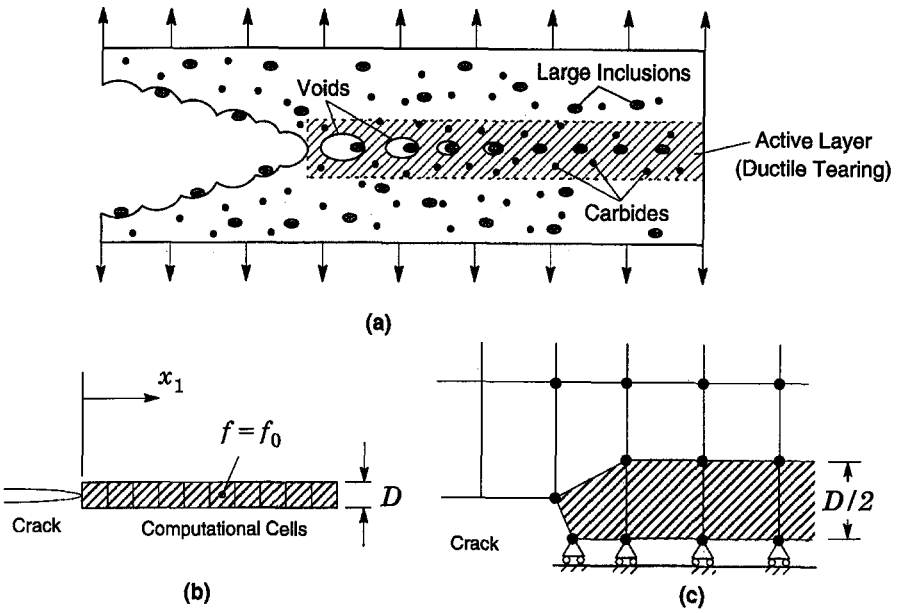

Figure 4. Modeling of ductile tearing using computational cells.

which drive the statistical treatment of cleavage fracture described previously, and which may accelerate the final stages of coalescence. Although the highly localized path followed by the crack front becomes generally non-planar and tortuous (i.e., alternate sliding-off), macroscopic growth reveals a simple planar character dictated by the symmetric, mode I loading. Moreover, negligible void growth occurs in material at distances from the crack plane of more than 1–2 × the spacing of larger inclusions. The distance ahead of the crack tip over which the microstructural voids experience active growth under increased loading of a specimen defines the fracture process zone for ductile tearing. A small process zone consisting of only a few voids leads to higher toughness, in terms of a $J - \Delta a$ curve, than does a larger process zone which exhausts much of the void growth capacity before the advancing tip reaches a void. Numerical results of X&S indicate that such process zones increase in size for rising R-curves, with steady-state growth ($dJ/da \rightarrow 0$) being reached when the process zone approaches a limiting size.

These observations led X&S to propose the computational model illustrated in Figure 4(b). Void growth remains confined to a layer of material symmetrically located about the crack plane and having thickness D, where D is associated with the mean spacing of the larger, void initiating inclusions. This layer consists of cubical cell elements with dimension D on each side; each cell contains a centered spherical cavity of initial volume fraction f_0 (the initial void volume divided by cell volume). As a further simplification, the void nucleates from an inclusion of relative size f_0 immediately upon loading. Progressive void growth and subsequent macroscopic material softening in each cell are described with the Gurson–Tvergaard (GT) constitutive model for dilatant plasticity [37, 38]. When f in the cell incident on the current crack tip reaches a critical value, f_E, the computational procedures remove the cell thereby advancing the crack tip in discrete increments of the cell size. Figure 4(c) shows the typical, plane strain finite element representation of the computational cell model where symmetry about the crack plane requires elements of size $D/2$. Material outside the computational cells,

the 'background' material, follows a conventional J_2 flow theory of plasticity and remains undamaged by void growth in the cells.

Material properties required for this methodology include: for the background material Young's modulus (E), Poisson's ratio (ν), yield stress (σ_0) and hardening exponent (n) or the actual measured stress-strain curve; and for the computational cells: D and f_0 (and of much less significance f_E). The background material and the matrix material of the cells generally have identical flow properties. Using an experimental $J - \Delta a$ curve obtained from a conventional SE(B) or C(T) specimen, a series of finite element analyses of the specimen are conducted to calibrate values for the cell parameters D and f_0 which bring the predicted $J - \Delta a$ curve into agreement with experiment. The CTOD at initiation of ductile tearing provides a good starting value for D, with f_0 then varied to obtain agreement with the experiment. Alternatively, metallurgical surveys of inclusion volume fractions and sizes may be used with various packing arrangements (e.g. nearest neighbor distance) to estimate D and/or f_0. Experience with plane strain finite element analyses of SE(B) and C(T) specimens to estimate D and f_0 for common structural and pressure vessel steels suggests values of 50–200 μm for D, 0.001–0.005 for f_0, with f_E typically 0.15–0.20. Once determined in this manner using a specific experimental R-curve, D and f_0 become 'material' parameters and remain fixed in analyses of all other specimen geometries for the same material.

In their initial work, X&S [33] describe systematic parametric studies of material flow properties and the cell parameters, D and f_0, on crack-tip stress fields and R-curves for SSY conditions and for a wide array of fracture specimens modeled in plane strain. They show that R-curves have increased toughness with increased D at fixed f_0 whereas for a fixed D and increased f_0, the R-curves show decreased toughness. These model predictions are in accord with experimental observations of material microstructure effects on R-curves. In Part II [35], they demonstrate the negligible effect on R-curves of stress-controlled nucleation of the initial void, the ability of the cell model to capture the averaged effects of highly localized, zig-zag fracture, and the small influence on R-curves of strain-controlled, new void nucleation during the final stage of growth.

3.2. CONSTITUTIVE MODELS

To describe the evolution of void growth and associated macroscopic material softening in the computational cells, we adopt the Gurson [37] and Tvergaard [38] potential function (g) for plastic flow in porous media

$$g(\sigma_e, \sigma_m, \bar{\sigma}, f) = \left(\frac{\sigma_e}{\bar{\sigma}}\right)^2 + 2q_1 f \cosh\left(\frac{3q_2\sigma_m}{2\bar{\sigma}}\right) - (1 + q_3 f^2) = 0, \tag{9}$$

where σ_e denotes the effective Mises (macroscopic) stress, σ_m is the mean (macroscopic) stress, $\bar{\sigma}$ is the current flow stress of the cell matrix material and f defines the current void fraction. Under multiaxial stress states, $\sigma_e = (3S_{ij}S_{ij}/2)^{1/2}$, where S_{ij} denotes the deviatoric components of Cauchy stress expressed on a rotation neutralized material element (see Section 3.3). Factors q_1, q_2 and q_3 introduced by Tvergaard improve the model predictions for periodic arrays of cylindrical and spherical voids; here we use $q_1 = 1.25, q_2 = 1.0$ and $q_3 = q_1^2$.

The internal state variables for the constitutive model are thus f and $\bar{\sigma}$. The instantaneous growth rate of cell voids is given by

$$\dot{f} = (1 - f)\dot{\varepsilon}^p_{kk} + \mathcal{A}\dot{\bar{\varepsilon}} + \mathcal{B}(\dot{\bar{\sigma}} + \dot{\sigma}_m), \tag{10}$$

where in the present analyses $\mathcal{A} = \mathcal{B} \equiv 0$ to suppress the formation of new voids in the final stages of growth by plastic strain ($\mathcal{A}$) and early in the loading when stress triaxiality on cells remains high ($\mathcal{B}$). By enforcing equality between the rates of macroscopic and matrix plastic work, the matrix stress, $\bar{\sigma}$, becomes coupled to the plastic strain rate in the matrix material through

$$\dot{\bar{\varepsilon}} = \frac{\boldsymbol{\sigma} : \dot{\boldsymbol{\varepsilon}}^p}{(1-f)\bar{\sigma}}, \tag{11}$$

where $\bar{\sigma}(\bar{\varepsilon})$ also follows a prescribed hardening function for the matrix material.

The GT constitutive model does not predict a realistic loss of macroscopic stress in a cell at large void fractions, e.g. $f > 0.15$. Tvergaard and Needleman [61] introduced an accelerated value of f, f^*, when $f \approx 0.15$ to overcome this difficulty. An element extinction procedure (proposed by Tvergaard) also offers a simple alternative. When the averaged value of f at the Gauss points in a cell element reaches f_E, the cell stiffness is made zero and the remaining stresses are relaxed to zero following a linear traction-separation model (here we reduce the stresses linearly to zero over an additional 10 percent elongation of the cell normal to the crack plane). Effects of the specific extinction process diminish quickly when the number of load increments used in an analysis limits the number of cells undergoing extinction to just one or two. Based upon previous analyses [33, 47], f_E is here assigned the value of 0.20.

The background material outside of the computational cells follows a J_2 flow theory with the Mises plastic potential obtained by setting $f \equiv 0$ in (9). The uniaxial true stress-logarithmic strain response for both the background and cell matrix materials follows a simple power-hardening model,

$$\frac{\varepsilon}{\varepsilon_0} = \frac{\bar{\sigma}}{\sigma_0} \quad \varepsilon \leqslant \varepsilon_0; \qquad \frac{\varepsilon}{\varepsilon_0} = \left(\frac{\bar{\sigma}}{\sigma_0}\right)^n \quad \varepsilon > \varepsilon_0, \tag{12}$$

where σ_0 and ε_0 are the reference (yield) stress and strain, and n is the strain hardening exponent. Section 4 describes numerical solutions for the SSY boundary-layer model with nonzero T-stress using materials with $n = 5$ (high hardening), $n = 10$ (moderate hardening) and $n = 20$ (low hardening). The initial linear stress-strain response included in (12) becomes necessary at high $|T/\sigma_0|$ ratios to maintain a linear-elastic response in the remote field. Section 5 describes numerical analyses for SE(B) specimens that were tested in the experimental program. The true stress-logarithmic strain behavior for the high-strength, low hardening material of these specimens is modeled with a piecewise linear approximation to the measured response as shown in Figure 10(a).

3.3. Finite element procedures

Finite element solutions are generated using the WARP3D code [48] which:

(1) implements the GT and Mises constitutive models in a finite-strain framework,
(2) provides automatic cell extinction coupled to the GT model, and
(3) evaluates the J-integral using a convenient domain integral procedure.

Although the present analyses involve plane-strain conditions, these features are all available for solution of large-scale 3-D models. The nonlinear implementation of the finite element method in WARP3D employs a continuously updated formulation naturally suited for solid

elements having only translational displacements at the nodes. The principle of virtual work expressed on the current configuration, denoted $n+1$, has the form

$$\int_{V_{n+1}} \delta\boldsymbol{\varepsilon} : \boldsymbol{\sigma}_{n+1}\, \mathrm{d}V - \delta\bar{\mathbf{u}}^T \mathbf{P}_{n+1} = 0, \tag{13}$$

where $\boldsymbol{\sigma}_{n+1}$ denotes the Cauchy stress, $\mathbf{P}$ contains the external nodal forces acting on the model at $n+1$, $\delta\bar{\mathbf{u}}$ defines virtual displacements at the nodes and $\delta\boldsymbol{\varepsilon}$ represents the symmetric, rate of the virtual deformation tensor relative to the current configuration, i.e., $\delta\boldsymbol{\varepsilon} = \mathrm{sym}(\partial\delta\mathbf{u}/\partial\mathbf{x}_{n+1})$.

Starting from (13) linearized about the current configuration, the global solution proceeds in an incremental-iterative (implicit) manner with nodal equilibrium stringently enforced at $n+1$. Each Newton iteration to advance the solution from $n \rightarrow n+1$ employs the (consistent) tangent stiffness computed for the current estimate of the solution at $n+1$. Final increments of logarithmic strain over $n \rightarrow n+1$ are then evaluated using the linear strain-displacement matrix evaluated on the converged mid-increment configuration $\mathbf{x}_{n+1/2}$.

WARP3D analyzes fracture models constructed with three-dimensional, 8-node tri-linear hexahedral elements. Use of the so-called $\bar{\mathbf{B}}$ formulation [49] precludes mesh lock-ups that arise as the deformation progresses into fully plastic, incompressible modes. Dilatational terms of the original strain-displacement matrix are replaced by a volume averaged set of dilatational terms which yield uniform mean stress over the element and minimal locking. To achieve plane-strain models for the current study, a single thickness layer of the 3-D elements is defined with out-of-plane displacements constrained to vanish.

To accommodate finite strains and rotations, the GT and Mises constitutive equations are formulated using strains-stresses and their respective rates defined on an *unrotated* frame of reference, computed from polar decompositions of the deformation gradients ($\mathbf{F} = \mathbf{RU}$). The stress-update proceeds as follows (see [59] for full details):

(1) using $\mathbf{R}_{n+1/2}$ rotate the spatial increment of the deformation tensor ($\mathbf{D}$), evaluated from $\bar{\mathbf{B}}_{n+1/2} \cdot \Delta\bar{\mathbf{u}}_e$, to the unrotated configuration, $\mathbf{d}_{n+1/2} = \mathbf{R}^T_{n+1/2}\mathbf{D}_{n+1/2}\mathbf{R}_{n+1/2}$;
(2) compute the unrotated Cauchy stress at $n+1(\mathbf{t}_{n+1})$ using a convensional small-strain, backward Euler procedure; and
(3) compute the spatial Cauchy stress at $n+1$ as $\boldsymbol{\sigma}_{n+1} = \mathbf{R}_{n+1}\mathbf{t}_{n+1}\mathbf{R}^T_{n+1}$.

The polar decompositions insure accuracy in the rotational operations independent of the displacement gradient magnitudes over $n \rightarrow n+1$. Our implementation of the backward Euler integration scheme for the GT model builds upon Aravas's work [57]. The linearized form of (13) requires a tangent operator which couples the spatial rates of Cauchy stress $\dot{\sigma}_{n+1}$ and deformation tensor $\dot{\varepsilon}_{n+1}$. The procedure adopted here follows that described by Nagtegaal and Veldpaus [58], which uses the exact consistent tangent operator on the unrotated configuration $\mathbf{E} = (\partial\mathbf{t}/\partial\mathbf{d})_{n+1}$, the instantaneous rotation rate at the material point ($\boldsymbol{\Omega} = \dot{\mathbf{R}}\mathbf{R}^T$), and the Green–Naghdi rate of the spatial Cauchy stress ($\dot{\boldsymbol{\sigma}}_{GN} = \dot{\boldsymbol{\sigma}} - \boldsymbol{\Omega}\boldsymbol{\sigma} + \boldsymbol{\sigma}\boldsymbol{\Omega}$).

The *local* value of the mechanical energy release rate at a stationary crack tip in plane strain is given by

$$J = \lim_{\Gamma_0 \rightarrow 0} \int_{\Gamma_0} \left[\mathcal{W} n_1 - P_{ji} \frac{\partial u_i}{\partial X_1} n_j \right] \mathrm{d}\Gamma_0 \tag{14}$$

where Γ_0 denotes a contour defined on the undeformed configuration ($t = 0$) beginning at the bottom crack face and ending on the top face, n_j is the outward normal to Γ_0, $\mathcal{W}$ denotes the

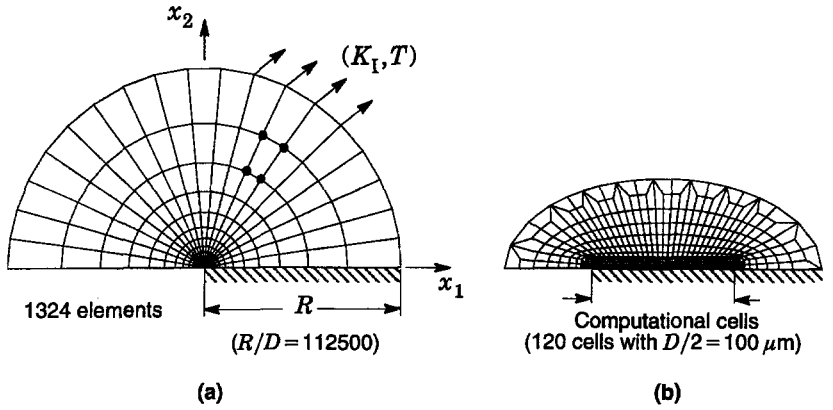

Figure 5. Small scale yielding model; (a) finite element mesh of upper half of semi-infinite crack; (b) crack-tip region contain a single layer of computational cells.

stress-work density per unit of undeformed volume, P_{ij} and u_i are Cartesian components of (unsymmetric) Piola–Kirchoff stress and displacement in the crack front coordinate system. Our finite element computations employ a domain integral procedure [50] for numerical evaluation of (14). For crack tips experiencing stable ductile growth, J is evaluated over domains outside the highly non-proportional histories of the near-tip fields and thus retains a strong domain (path) independence. Such J-values are in accord with experimental estimation schemes, and they provide a convenient parameter to characterize intensity of far field loading on the crack tip.

3.4. SMALL SCALE YIELDING MODEL

The modified boundary layer model [62, 63] simplifies the generation of numerical solutions for stationary and growing cracks under well-defined SSY conditions with varying levels of constraint. Figure 5 shows the plane-strain finite element model for an infinite domain, single-ended crack problem; mode I loading of the far field permits analysis using one-half of the domain as shown. With the plastic region limited to a small fraction of the domain radius, $R_p < R/20$, the general form of the asymptotic crack-tip stress fields well outside the plastic region is given by [51]

$$\sigma_{ij} = \frac{K_I}{\sqrt{2\pi r}} f_{ij}(\theta) + T\delta_{1i}\delta_{1j}, \tag{15}$$

where K is the stress intensity factor, $f_{ij}(\theta)$ define the angular variations of in-plane stress components, and the nonsingular term T represents a tension (or compression) stress parallel to the crack. Numerical solutions for different levels of T/σ_0 are generated by imposing displacements of the elastic, mode I singular field on the outer circular boundary ($r = R$) which encloses the crack

$$u(R,\theta) = K_I \frac{1-\nu}{E}\sqrt{\frac{R}{2\pi}}\cos(\tfrac{1}{2}\theta)(3 - 4\nu - \cos\theta) + T\frac{1-\nu^2}{E}R\cos\theta, \tag{16}$$

$$v(R,\theta) = K_I \frac{1-\nu}{E}\sqrt{\frac{R}{2\pi}}\sin(\tfrac{1}{2}\theta)(3 - 4\nu - \cos\theta) - T\frac{\nu(1-\nu)}{E}R\sin\theta. \tag{17}$$

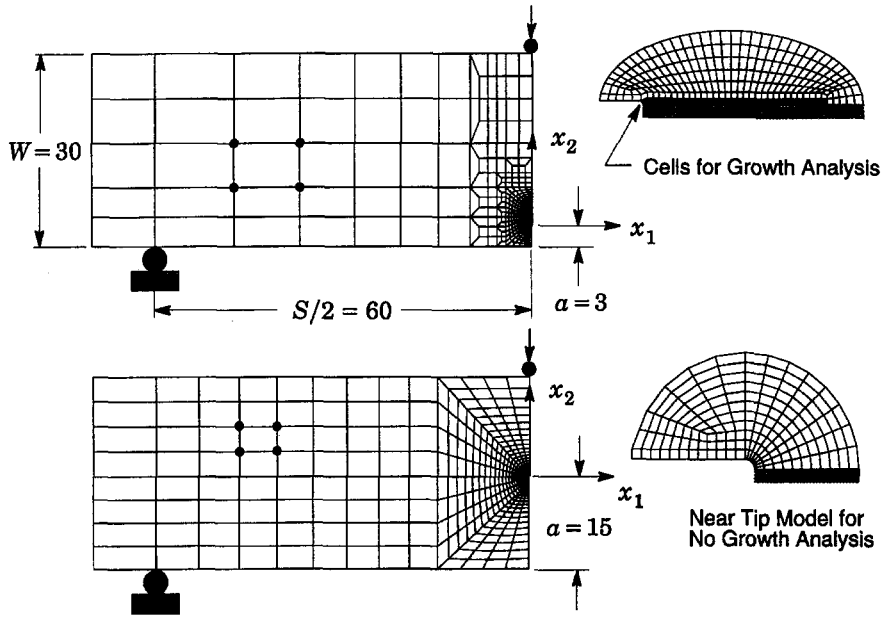

Figure 6. Finite element models for three-point SE(B) specimens; (a) $a/W = 0.1$; (b) $a/W = 0.5$ (all units in mm).

For crack growth analyses, the model has a single layer of 120 computational cells along the crack plane, with the plastic behavior of each cell as described in Section 3.2. These computational cells have a fixed size of $D/2 \times D/2$, with $D = 200\mu$m and $R/D = 112500$. Figure 4(c) shows the initial crack-tip geometry for the growth analyses. The parametric effects of cell size on near-tip fields and resistance curves are not addressed in the present study (see X&S [33–35] for comparative solutions). In general, for a given amount of crack growth under steady state conditions, the J scales directly with $D\sigma_0$ and inversely with f_0.

Stationary crack analyses employ the same element mesh but with no damage in the cells. In both stationary and growth analyses, the initial crack-tip radius of $D/2$ provided by the cell incident on the tip provides two numerical benefits:

(1) it accelerates convergence of the finite-strain plasticity algorithms during the initial stage of blunting, and
(2) it minimizes numerical problems during computation of the Weibull stress over material incident on the crack tip.

The SSY model has one thickness layer of 1300 8-node, 3-D elements; with plane-strain constraint imposed, the model has 4000 nodal displacements. A typical solution to grow the crack for 20 cells using 1000 load increments requires 3–4 hours of CPU time on a desktop (HP) workstation.

3.5. PLANE-STRAIN SE(B) SPECIMENS

Finite element analyses are conducted on conventional plane-sided SE(B) specimens $W/S = 4$ with $a/W = 0.1$ and $a/W = 0.5$ (W is the width and S is the span for the bend specimens). The geometry, size and material flow properties match those for specimens tested

in the experiments described in Section 5. Figure 6 shows the finite element models for both a/W ratios. Symmetry conditions permit modeling of only one-half of the specimen with appropriate constraints imposed on the remaining ligament. Stationary and growing crack analyses for these specimens generate detailed descriptions of the near-tip stress fields used to construct the proposed toughness scaling model.

Testing of the deeply notched bend specimens yielded fracture toughness values exhibiting a well-defined cleavage mode with no stable crack growth. For these specimens, a conventional mesh configuration having a focused ring of elements surrounding the crack front is used with a small key-hole at the crack tip (radius of 100 μm to maintain similar near-tip refinement with the computational cell mesh). The mesh has 480 elements with sufficient refinement near the tip to provide adequate resolution of the stress fields. For the shallow notched specimens, ductile tearing prior to cleavage fracture is observed in the experiments and requires a mesh with computational cells ahead of the crack front (see Section 3.2). The finite element model has 30 computational cells with $D/2 = 100\,\mu$m in an arrangement similar to the SSY model previously discussed. This mesh contains 600 elements. For comparison, a finite element analysis of a stationary crack is also conducted for the shallow notched specimen. The mesh details are similar to those for the deep notch specimen.

The models are loaded by displacements imposed on the top 2–3 nodes on the symmetry plane. To insure load step independence of the results, the analyses use 650 load increments to grow the crack by 25 cells ($\Delta a = 2.5$ mm).

3.6. Numerical computation of the Weibull stress

This section briefly summarizes the finite element form of the Weibull stress expression for a stationary and a growing crack, (4) and (7), employed in these analyses. In parametric space, the current (deformed) Cartesian coordinates x_i of any point inside a 8-node tri-linear element are related to the parametric coordinates η_i through the relationship [52]

$$x_i = \sum_{k=1}^{8} N_k x_{ik}, \quad i = 1,2,3, \tag{18}$$

where N_k are the shape functions corresponding to node k and x_{ik} are the current (deformed) nodal coordinates, $x_i = X_i + u_i$. The shape functions have standard form

$$N_k = \frac{1}{8}\prod_{i=1}^{3}(1 + \eta_i\eta_{ik}), \quad k = 1,\ldots,8, \tag{19}$$

where η_{ik} denotes the parametric coordinates of node k.

Let $|J|$ denote the determinant of the standard coordinate Jacobian between deformed Cartesian and parametric coordinates. Then using standard procedures for integration over element volumes, the Weibull stress has the form

$$\sigma_w = \left[\frac{1}{4\pi V_0}\sum_{n_e}\int_{\Omega_e}\int_0^{2\pi}\int_0^{\pi}\sigma^m \sin\phi\,\mathrm{d}\phi\,\mathrm{d}\theta\,\mathrm{d}\Omega_e\right]^{1/m} \tag{20}$$

$$= \left[\frac{1}{4\pi V_0}\sum_{n_e}\int_{-1}^{1}\int_{-1}^{1}\int_{-1}^{1}\int_0^{2\pi}\int_0^{\pi}\sigma^m|J|\sin\phi\,\mathrm{d}\phi\,\mathrm{d}\theta\,\mathrm{d}\eta_1\,\mathrm{d}\eta_2\,\mathrm{d}\eta_3\right]^{1/m}, \tag{21}$$

where n_e is the number of elements inside the fracture process zone near the crack tip and Ω_e is the volume of the element. The process zone used here includes all material inside the loci $\sigma_1 \geqslant \lambda\sigma_0$, with $\lambda = 2$. For computational simplicity, an element is included in the fracture process zone if the σ_1 computed at $\eta_1 = \eta_2 = \eta_3 = 0$ exceeds $2\sigma_0$.

Application of (21) requires a specific definition for the tensile stress, σ, acting on the microcrack. This tensile stress can be determined for each pair of coordinates (θ, ϕ) by using one of several proposed fracture criteria coupled with a geometric shape for the microcrack [15, 24, 28]. However, little agreement exists about which criterion most effectively describes cleavage fracture. Consequently, we adopt the simple, maximum principal tensile stress criterion to describe unstable crack propagation. Upon replacing the tensile stress σ in (21) with the maximum principal stress σ_1 which acts on the material volume element, the Weibull stress takes the form

$$\sigma_w = \left[\frac{1}{V_0}\sum_{n_e}\int_{-1}^{1}\int_{-1}^{1}\int_{-1}^{1}\sigma_1^m |J|\,\mathrm{d}\eta_1\,\mathrm{d}\eta_2\,\mathrm{d}\eta_3\right]^{1/m} \tag{22}$$

which reflects the independence of the principal stress on the curvilinear coordinates (θ, ϕ). This expression for the Weibull stress represents the integral form in parametric space of Beremin's formulation [17].

4. Fracture resistence behavior under SSY conditions

Small-scale yielding analyses under varying levels of T-stress provide valuable insight about the effects of crack-tip constraint and ductile tearing on fracture resistance. Here we focus on the evolution of Weibull stress with crack-tip stress triaxiality and crack growth. A central feature of the present investigation involves the interpretation of σ_w as a *macroscopic* crack driving force and the implications of its use in assessments of brittle fracture behavior. These SSY results exhibit the essential features of our micromechanics approach in correlating macroscopic fracture toughness with constraint variations and ductile tearing.

4.1. The Weibull stress for stationary cracks

Small-scale yielding solutions with varying levels of applied T-stress are generated for power-law hardening materials having three levels of strain hardening ($n = 5, 10, 20$) each with $E/\sigma_0 = 500, \nu = 0.3$. These properties characterize a relatively wide range of plastic behavior for structural and pressure vessel steels with moderate-to-high strength. In each analysis, the full value of T-stress is imposed first (which causes no yielding), followed by the K_I field imposed in an incremental manner. For convenience, a *reference* unit thickness $B = 1$ is used throughout.

In evaluating the Weibull stress, (22), under increasing K_I levels, three values of the shape parameter are considered: $m = 10, 20$ and 30. In particular, $m \approx 20$ characterizes the distribution of Weibull stress at cleavage fracture for a nuclear pressure vessel steel (ASTM A508) [17]. These values of m reflect different microcrack densities and thereby provide further insight into the fracture behavior for these materials.

Figure 7(a–c) shows the variation of Weibull stress under increasing deformation for the three levels of hardening $n = 5, 10, 20$ each with $m = 20$, and for values of T-stress ranging from $-0.75 \leqslant T/\sigma_0 \leqslant 0.5$. For $T/\sigma_0 = 0$ and fixed strain hardening ($n = 10$), Figure 7(d)

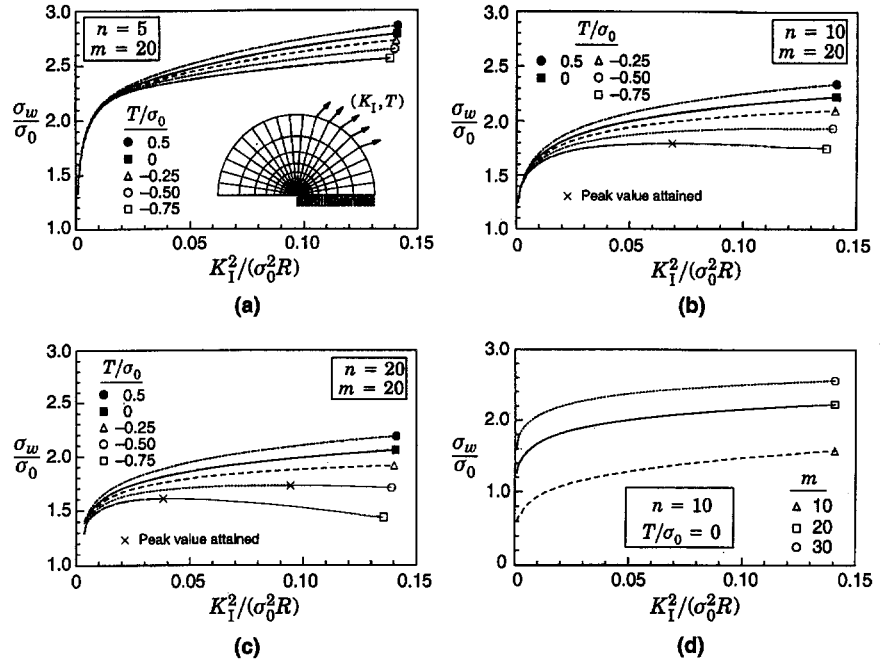

Figure 7. Stationary crack analysis under SSY conditions and varying hardening properties for $E/\sigma_0 = 500$ (Weibull stress is calculated using the instantaneous fracture process zone).

shows the variation of Weibull stress with increasing deformation for $m = 10, 20$ and 30. In these plots, $K_I^2/(\sigma_0^2 R)$ describes the far-field loading with the Weibull stress normalized by the yield stress, σ_0. The evolution of σ_w as deformation progresses depends markedly on the degree of strain hardening and T/σ_0. Positive values of T/σ_0 have a small effect at all hardenings levels. For all T/σ_0 levels, the Weibull stress for $n = 5$ increases steadily with deformation and remains well above the values for $n = 10$ and 20.

The most striking feature of these results, however, is the development of σ_w with increasing deformation for negative values of T in the materials with $n = 10$ and 20 (see Figures 7(b, c)). The Weibull stress in these materials increases at a much lower rate with increasing deformation, especially for the low hardening material in the range $-0.75 \leqslant T/\sigma_0 \leqslant -0.5$. Under these conditions of severe constraint loss, there develops early in the loading a maximum value of σ_w indicated by a marker $(\times)$ on these curves. At higher remote loading but with continuing constraint loss, the Weibull stress based on the instantaneous process zone (see Section 2.2) decreases due to the lower near-tip stresses. In the post-peak regime, σ_w as defined here cannot describe a realistic failure probability for the cracked body, which must continue to increase possibly by the intervention of ductile tearing as demonstrated in the following section. Similar observations and comments are made by Mudry [22] based on numerical plane-strain analyses of fracture specimens with low strain hardening rates under large scale yielding. In contrast, σ_w for $n = 5$ increases monotonically over the full range of deformation analyzed for all values of T/σ_0, i.e., the increased stresses provided by hardening more than offset the loss in stress triaxiality. These results demonstrate clearly the strong effect of constraint loss $(T/\sigma_0 < 0)$ on the levels of σ_w for moderate-to-low hardening materials. The effects of T/σ_0 on σ_w observed here are entirely consistent with the J-Q characterization of SSY stress fields described by O'Dowd and Shih [12, 13]. The lower σ_w-values with

$T/\sigma_0 < 0$ follow from the reduced stress triaxiality levels ahead of the crack tip, as described by negative Q-values. These trends remain relatively independent of the m-value adopted, as can be seen in Figure 7(d). Here, m simply scales the magnitude of Weibull stress after the early stages of loading in accordance with $\sigma_w = \beta_m K_{\mathrm{I}}^{4/m}$ [22], where the proportionality constant, β_m, depends on m.

In summary, the micromechanics approach adopted here postulates that cleavage fracture occurs when the Weibull stress reaches a critical value σ_{wc} which is a material dependent property. The analysis results shown in Figure 7 demonstrate that attainment of σ_{wc} for low constraint crack configurations occurs, if at all, only at much greater deformation levels (K_{I}) relative to high constraint configurations. Moreover, the combination of a low strain hardening material and a low constraint crack configuration may never generate $\sigma_w = \sigma_{wc}$, in which case cleavage fracture cannot occur unless some other event (e.g., ductile tearing) elevates the near-tip stresses.

4.2. Effects of ductile tearing on the Weibull stress

The previous results demonstrate a significant reduction of the Weibull stress under low constraint conditions (negative T-stress) for low and moderately hardening materials. This section examines the potential for ductile tearing to counteract the effects of constraint loss and thus restore the Weibull stress to high constraint levels – such an outcome would aid in explaining the transition from a stable ductile tearing mode to a cleavage mode of fracture. To conserve space, we describe only key results computed for $m = 20$ (shape parameter) and $f_0 = 0.001, 0.005$ (initial void fraction for the material). Similar trends and conclusions are drawn for other m and f_0 values. For the strongly negative T-stress levels, these analyses typify cleavage fracture accompanied by small amounts of stable crack growth of structural steels in low-constraint configurations. In the context of our computational cell model, values of f_0 (0.001–0.003) and cell sizes of $D \approx 200\,\mu$m characterize materials with moderate crack growth resistance [33, 47].

Figures 8(a, c) show the computed crack growth resistance curves for materials having $m = 10, 20$ and $f_0 = 0.001$. J is normalized by the cell size and flow stress ($D\sigma_0$) while Δa is normalized by D. The cell with current porosity $f = 0.1$ defines the current crack tip location, and thus Δa. This 'operational' definition locates the crack tip in the region behind the peak stress where stresses decrease rapidly, but ahead of the very highly damaged region, where the GT model does not accurately predict material response. Figures 8(b, d) present the dependency of σ_w, (22), on crack growth. For all levels of crack-tip constraint represented by T/σ_0, the Weibull stress increases monotonically with ductile extension (compare Figures 8b, d with the nogrowth results in Figures 7b, c). The levels of σ_w for the material with $n = 20$ remain consistently lower than the levels for the material with $n = 10$ at the same value of T/σ_0 and crack extension. These results clearly reflect the less severe near-tip stresses that develop for the $n = 20$ material and for low-constraint conditions. The computed R-curves at large growth reveal a different trend of lower toughness with higher strain hardening for all constraint levels. The computational results here for $f_0 = 0.005$ are fully consistent with those of X&S [33] (they did not consider $f_0 = 0.001$ for these cases).

For a fixed cell size, Figure 9 illustrates the interaction between strain hardening and initial porosity for large amounts of crack extension. In these analyses $T/\sigma_0 = 0$. Figures 9(a, b) present computed R-curves for materials with $n = 5, 10, 20$ and initial volume fractions of $f_0 = 0.001, 0.005$. Figures 9(c, d) provide the corresponding distribution of opening-mode

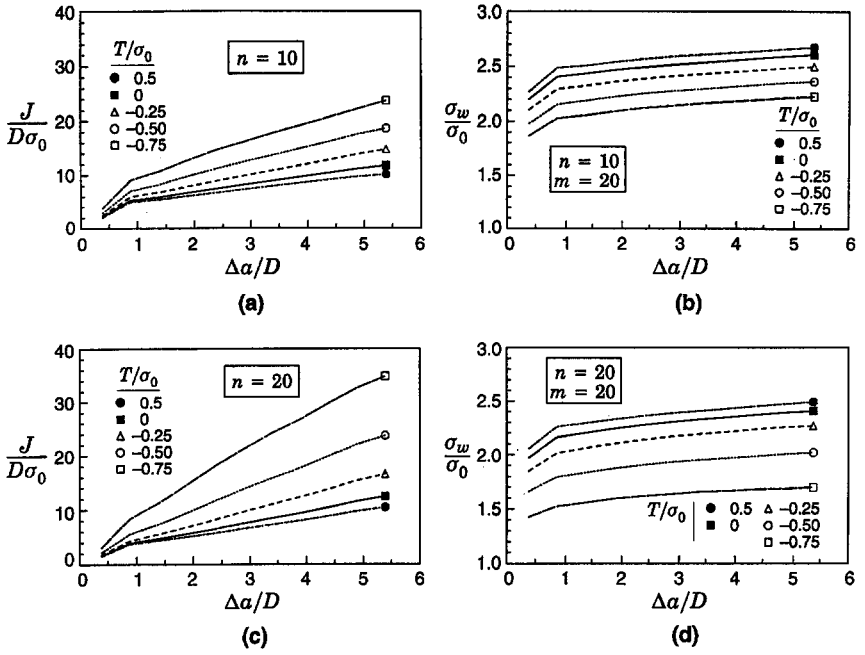

Figure 8. Crack growth analyses under SSY conditions and varying hardening properties for $E/\sigma_0 = 500$ and $f_0 = 0.001$ (Weibull stress is computed using the instantaneous fracture process zone).

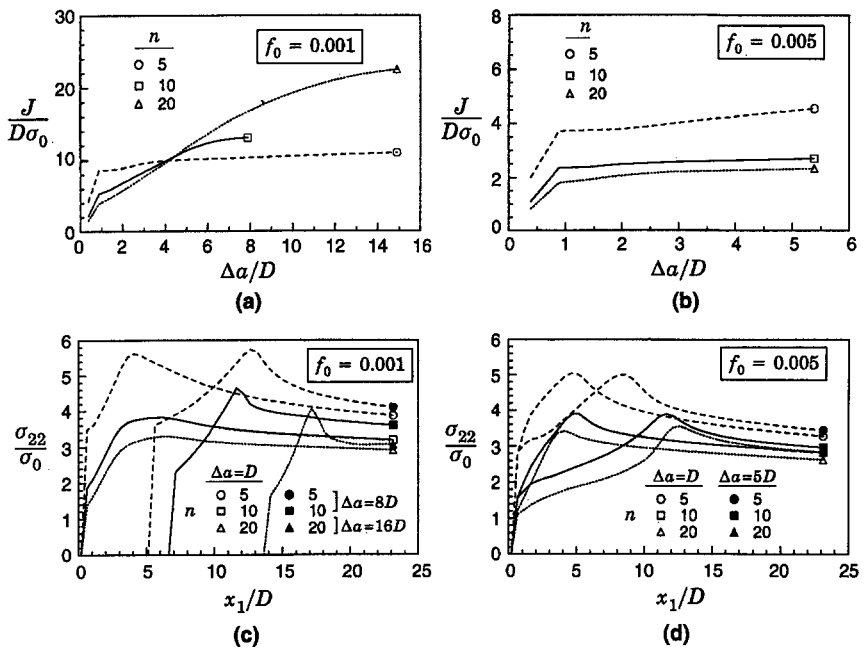

Figure 9. Crack growth analyses under SSY conditions for different values of initial void fraction ($T/\sigma_0 = 0$).

tensile stress σ_{22} at distances measured from the original crack tip, x_1, for different amounts of crack growth. For all of the $f_0 = 0.005$ analyses, essentially steady-growth conditions ($dJ/da \to 0$) develop after only a few cells of crack extension. The steady-growth J-values

(J_{ss}) increase with increased strain hardening levels. Similarly, computed values of J_{Ic} show a consistently increasing trend with increased strain hardening, where J_{Ic} here is taken as the J-value at $\Delta a/D \approx 1$. The computed R-curves for the $f_0 = 0.001$ analyses reveal a different character – J_{ss} levels are reversed with respect to strain hardening ($n = 20$ now has the largest J_{ss}), and much greater amounts of crack growth are needed for the $n = 10, 20$ solutions to reach steady conditions. However, J_{Ic} values vary with strain hardening as for the $f_0 = 0.005$ analyses.

The stress distributions shown in Figures 9(c, d) aid in understanding these trends. A rising R-curve is identified with an opening mode stress that exhibits an increasing peak value with growth and an increasingly larger distance between the crack tip and the location of peak stress. Steady-growth conditions exhibit a constant peak stress value during further growth and an essentially fixed distance between the peak stress location and the crack tip. For all cases but $f_0 = 0.001$ with $n = 10, 20$, steady-conditions develop after only 1–2 cells of growth. Under these conditions, the low degree of hardening coupled with the much smaller initial porosity requires significant growth before the peak stress attains a level that accelerates void growth. Consider the development of opening-mode stresses for the $n = 20$ material; the peak stress increases from $3.2\sigma_0$ to $4.2\sigma_0$ following 16 cells of growth, after which steady conditions appear to exist. In contrast, J_{Ic} depends entirely on the response of the cell adjacent to the blunting crack tip. Here, the development of plastic strains plays a key role in void growth since the traction free, blunted tip lowers the opening mode stress. For the same imposed J-value before growth, the $n = 5$ material has the smallest plastic strains while the $n = 20$ material has the largest plastic strains; consequently the largest J_{Ic} occurs for $n = 5$ with both small and large values of f_0.

Xia and Shih [33] and Xia, Shih and Hutchinson [34] discuss these constraint, strain hardening and initial porosity effects on R-curves in terms of the process zone for ductile fracture, defined as the material between the current physical crack tip and the cell carrying the largest opening stress. Material within this region undergoes severe damage due to void growth; the cells carry a reduced stress thereby exerting lower tractions on the surrounding material. The length of this (ductile) fracture process zone, l, strongly influences the tearing resistance. A small l/D implies a localized mechanism providing high toughness in which only one or two voids interact with the crack tip – the crack tip must advance to a cell before significant damage occurs. Larger values of l/D describe a lower-toughness mechanism in which many cells ahead of the advancing (physical) tip undergo damage well before the tip reaches them. From this viewpoint, the various steady-growth behaviors displayed in Figures 9(a, b) for different hardening and initial porosities correlate directly with the length of the fracture process zone. The opening-mode stresses at large amounts of growth, provided in Figures 9(c, d), clearly show the ordering of process zone sizes reflects the ordering of toughness levels at steady-growth conditions. The smallest process zone (and highest toughness) exists for the $n = 20, f_0 = 0.001$ material.

In summary, these representatives analyses demonstrate important features associated with the evolution of Weibull stress for a growing crack. The physical significance is this: ductile tearing increases the crack-tip driving force (σ_w) as deformation progresses particularly so for low-constraint configurations, which increases the likelihood of unstable crack propagation by cleavage. The trends shown here are consistent with those obtained in previous numerical analyses [28, 29] in that stable crack growth elevates the near-tip stresses and increases the volume of the cleavage fracture process zone. Since σ_w explicitly incorporates the crack-tip

Table 1. Chemical composition of tested QT steel (mass %)

C	Si	Mn	P	S	Cu	Ni	Cr	Mo	V	Al	Ti	B
0.10	0.27	1.11	0.007	0.002	0.02	0.31	0.12	0.16	0.04	0.067	0.009	0.0008

Table 2. Mechanical properties of tested QT steel at room temperature

σ_{ys} (MPa)	σ_u (MPa)	ε_t (%)	σ_u/σ_{ys}
663	716	9.0	1.08

σ_{ys} : 0.2% proof stress;
σ_u : ultimate tensile strength;
ε_t : uniform elongation (gage length = 32 mm).

stress field and the volume of the near-tip stressed material, it fully captures the governing features for cleavage fracture in growing cracks.

5. Application to fracture toughness testing

5.1. Experimental toughness data

Toyoda et al. [53] conducted CTOD fracture mechanics tests on SE(B) specimens (plane-sided) with a fixed overall geometry and varying crack length to width ratios a/W. The specimens have a loading span $S = 120$ mm, a width $W = 30$ mm, and thickness $B = 15$ mm (refer to Figure 6). The material is quenched and tempered (QT), HSLA steel (663 MPa yield stress) with relatively low strain hardening ($\sigma_u/\sigma_{ys} = 1.08$). Table 1 lists the chemical composition of this material, which may be termed 'clean' (low S content) relative to common pressure vessel and structural steels. Exceptionally high tearing resistance and low transition temperature may thus be anticipated. Mechanical tensile tests, conducted on a standard longitudinal tensile specimen (JIS number 4), provide the room temperature (20°C) stress-strain data. Table 2 also summarizes the mechanical properties obtained from these tests. Figure 10(a) shows the

Table 3. Weibull parameters for the QT steel calibrated from the SE(B) specimens with $a/W = 0.5$ and corresponding 90% confidence bounds

	m	σ_u (MPa)*
$\sigma_{th} = 0$	15.6 (9.0, 20.9)	1757 (1625, 1822)
$\sigma_{th} = 2\sigma_0$	3.4 (2.0, 4.6)	234 (155, 280)

*Estimated using $V_0 = 1$.

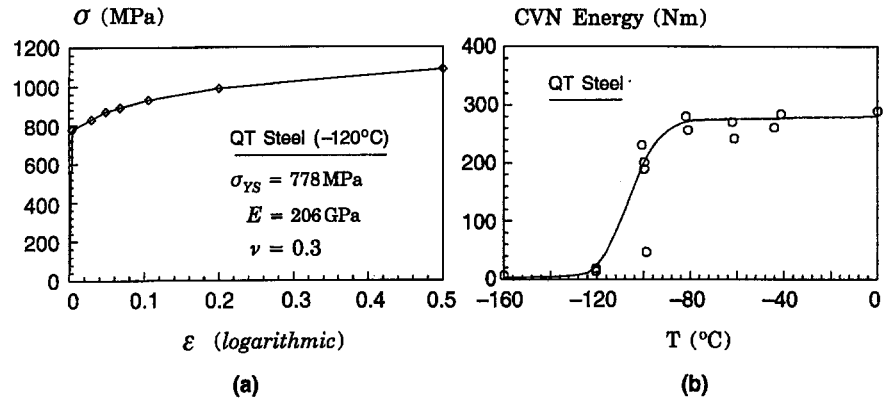

Figure 10. (a) Tensile data for QT steel employed at test temperature; (b) CVN transition curve.

true stress-logarithmic strain curve at test temperature ($-120°C$) for the material used in our finite element analyses of the SE(B) specimens. Figure 10(b) shows the measured toughness-temperature properties for the material in terms of conventional Charpy-V impact energy (L-T orientation).

In the present work, we limit attention to experimental data obtained for a deep crack ($a/W = 0.5$) and a shallow crack ($a/W = 0.1$) configuration. Testing of these configurations was carried out at $-120°C$ which corresponds to near lower-shelf behavior for the material with $a/W = 0.5$ (see CVN data in Figure 10b). Records of load *vs.* crack mouth opening displacements (CMOD) were obtained for each specimen using a clip gauge mounted on knife edges attached to the specimen surface. Post-test examinations established the amount of stable crack growth prior to final fracture by cleavage. Points along the crack front near the specimen surfaces were omitted in the averaging process, consistent with the plane-strain idealization employed in our analyses.

Using the measured plastic work defined by the plastic component of the area under the load versus CMOD curve, $A_{\rm pl}^{\rm CMOD}$, experimental fracture toughness values (J_c) are obtained using the estimation procedure described by Kirk and Dodds [54]. Experimental J_c-values are given by

$$J = \frac{K^2(1-\nu^2)}{E} + \frac{\eta_{J-C}}{Bb} A_{\rm pl}^{\rm CMOD}, \tag{23}$$

where the nondimensional *eta* factor for CMOD, rather than LLD, is given by

$$\eta_{J-C} = 3.75 - 3.101\frac{a}{W} + 2.018\left(\frac{a}{W}\right)^2, \qquad 0.05 \leqslant \frac{a}{W} \leqslant 0.70 \tag{24}$$

and b is the remaining ligament ($W - a$).

Figure 11(a) reveals the pronounced effect of a/W ratio and ductile growth on J_c-values. Most of the specimens with $a/W = 0.1$ experienced ductile crack extensions (Δa) of 0.5–0.75 mm prior to cleavage fracture. In contrast, specimens with $a/W = 0.5$ exhibited completely brittle behavior with no measurable crack extension prior to cleavage fracture. These results convincingly demonstrate the effect of severe constraint loss coupled with ductile tearing on the macroscopic fracture toughness, which leads to the increase in the

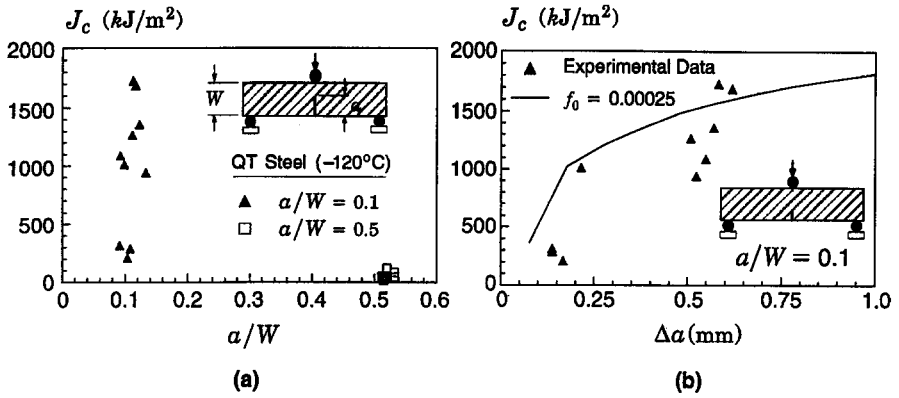

Figure 11. (a) Experimental cleavage fracture toughness data (SE(B) test results) for QT steel at –120°C. (b) Computed crack growth resistance curve for the SE(B) specimen with $a/W = 0.1$.

J_c-values for the shallow crack specimens. In the shallow-crack configuration, the near-tip opening mode stress levels fall precipitously when the global bending field impinges on crack-tip fields; attainment of a stress level sufficient to trigger cleavage becomes possible only at a greater deformation level. For specimens that fracture with very small amounts of crack extension ($\Delta a < 0.25$ mm, which is $\approx \delta_{Ic}$), the shallow-crack toughness exceeds the deep-crack toughness by a factor of 3–4. In other shallow-crack specimens, ductile tearing proceeds without triggering cleavage, pushing the fracture resistance much higher. Eventually, the re-elevated stress fields caused by the growth, coupled with the increased volume of crack-front material exposed to high stress levels, triggers cleavage. These specimens exhibit a 15–20 fold increase in toughness relative to the deep-crack specimens.

5.2. PREDICTION OF a/W AND Δa EFFECTS ON TOUGHNESS

The procedure used here to predict the combined effects of a/W ratio and ductile tearing for the experimental cleavage fracture toughness data follows the proposed scaling model outlined in Section 2.3 and illustrated in Figure 3. The notion of the Weibull stress as a crack-tip driving force establishes a function of the applied load and geometry which describes the local, crack-tip response for cleavage fracture. By postulating a critical value of the Weibull stress at fracture, the *distribution* of measured toughness values for one configuration may then be rationally employed to predict toughness distributions for other configurations. Here, we predict the distribution of cleavage fracture values for the shallow-crack specimens ($a/W = 0.1$) using the measured deep-crack toughness distribution to calibrate the scaling model.

The process begins by finding the material dependent value for the shape parameter, m, appearing in the Weibull stress as expressed by (22), or (4) for the general 3-D case. The numerical procedure for estimating the shape parameter m followed here is described fully in [25, 45]. This section includes a brief summary of the method which seeks to determine the parameters $\{m, \sigma_u\}$ of the probability distribution given by (5). Now, let $\mathcal{P}_{\text{fem}}(\sigma_w)$ and $\mathcal{P}_{\text{exp}}(\sigma_w)$ denote the distributions of σ_w corresponding to the stress state obtained through a finite element analysis and the one obtained through fracture toughness testing, respectively. By postulating that $\mathcal{P}_{\text{fem}}(\sigma_w)$ and $\mathcal{P}_{\text{exp}}(\sigma_w)$ have identical distributions, the calibration process becomes one of determining a set of parameters $\{m, \sigma_u\}$ which satisfies this condition. The

algorithm starts by determining $(\sigma_w)_{\text{fem}} = \text{F}(J, m)$ for an initial estimate of m, denoted m_0, where $\text{F}(J, m)$ denotes the computed functional relationship between J in the finite element model and the Weibull stress for the specified value of m [the curves in Figure 3(b) are given by $\text{F}(J, m)$]. The experimental Weibull stress $(\sigma_w)_{\text{exp}}$ corresponding to each experimental toughness value J_c is found by substituting J_c into $\text{F}(J, m)$. By applying a statistical analysis based upon the maximum likelihood method [55] to these $(\sigma_w)_{\text{exp}}$ values, the estimates $\{\hat{m}_1, (\hat{\sigma}_u)_1\}$ are found for the distribution $\mathcal{P}_{\text{exp}}(\sigma_w)$. If $m_0 \neq \hat{m}_1$, the process starts anew with the distribution $\mathcal{P}_{\text{fem}}(\sigma_w)$ computed for $m = \hat{m}_1$.

After convergence is attained, a small sample correction is applied to the maximum likelihood estimate of m using appropriate unbiasing factors given by Thoman et al. [56] (which are function of the number of cleavage fracture toughness data). As noted previously, the limiting distribution for the fracture stress is related explicitly to the distribution of the largest flaw in the material and is, therefore, also connected to the value of m. A general method through which this parameter can be directly determined without making recourse to microscale measurements relies upon an adequate analysis of a set of available experimental data. Here, the fracture toughness data for the SE(B) specimens with $a/W = 0.5$ are used. For the high-strength steel tested in these experiments, m has the calibrated value of 15.6. For comparison, we also conducted a similar analysis in which the threshold stress, σ_{th}, appearing in (3) is assigned a value of $2\sigma_0$. For this threshold stress, m has the calibrated value of 3.4. Table 3 summarizes the Weibull parameters corresponding to these two cases and also provides the 90 percent confidence bounds for the parameters based upon standard distributions of the maximum likelihood estimates given by Thoman et al. [56].

With the Weibull modulus m known, only the parameters to model ductile growth in the finite element analyses for this material remain unspecified. The computational cell approach requires calibration of the initial porosity f_0 and cell size D from a measured set of R-curves. Ideally, R-curves obtained using $a/W = 0.5$ specimens would be used for this procedure. However, deep-crack specimen R-curves are not available from the experimental investigation – at the test temperature, no ductile tearing occurs. R-curves at a higher temperature, if available, *might* be satisfactory for the calibration process by including the temperature dependence of the stress-strain curve. Alternatively, experimental R-curves for other, low constraint geometries would be suitable to perform the calibration. Here, only the shallow-crack data is available and we use it to perform calibration of the computational cell parameters (D, f_0).

Figure 11(b) shows the measured cleavage fracture data for the shallow-crack specimens plotted in an R-curve format. The computed resistance curve shown on this figure is obtained using the values $D = 200\,\mu\text{m}$ and $f_0 = 0.00025$ in the finite element analysis for ductile crack growth as described in Section 3.2 with $f_E = 0.15$. This very low value for f_0 reflects the exceptionally fine microstructure of this material which produces the very high tearing resistance under sustained growth. Despite the relative scatter observed in the experimental (cleavage) values, the predicted R-curve captures the average evolution of crack growth. Since the primary interest lies in generating the accompanying near-tip stress fields for the growing crack, this calibrated model appears satisfactory.

Figures 12(a–b) show the computed evolution of Weibull stress under increasing values of J for the deep and shallow crack configurations using the previous values for the threshold stress, i.e., $\sigma_{\text{th}} = 0$ and $\sigma_{\text{th}} = 2\sigma_0$. These curves provide the quantitative basis to predict the distribution of shallow-crack fracture toughness data from the measured distribution of deep-crack data. To illustrate the pronounced effect of ductile growth, Figures 12(a–b) also include the Weibull stress computed for the shallow-crack configuration *neglecting* growth.

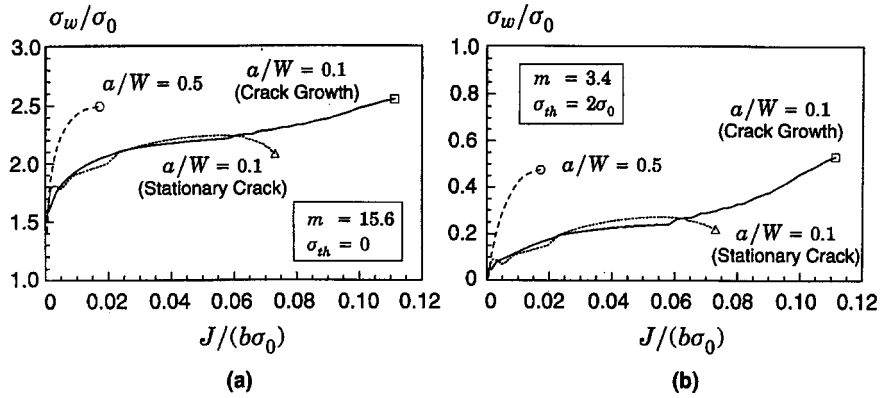

Figure 12. Variation of the Weibull stress σ_w with increasing load for the SE(B) specimens with two different values of threshold stress, σ_{th}. (a) Conventional definition of σ_w with $\sigma_{\text{th}} = 0$. (b) σ_w is calculated upon setting $\sigma_{\text{th}} = 2\sigma_0$.

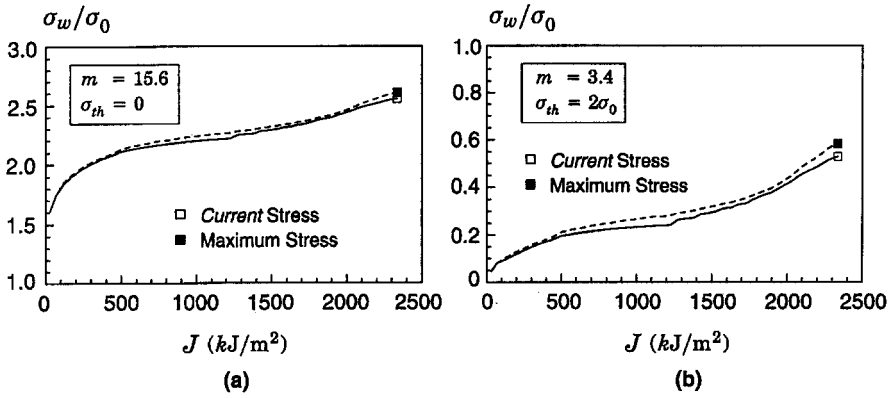

Figure 13. Variation of the Weibull stress σ_w with increasing load for the SE(B) specimens using the current stress (instantaneous fracture process zone) and the maximum stress experienced by a material element. (a) Conventional definition of σ_w with $\sigma_{\text{th}} = 0$. (b) σ_w is calculated upon setting $\sigma_{\text{th}} = 2\sigma_0$.

A marked decrease in the Weibull stress for the no growth analysis at $J/(b\sigma_0) \approx 0.05$ signals a sharp drop in near-tip constraint. While both growth and no-growth curves for the shallow crack configuration agree well at lower values of J, the behavior displayed by the stationary crack analysis clearly fails to predict the larger J_c-values measured in the experiments.

The Weibull stress values in these analyses derive from the *current* near-tip stress field (as provided by our definition of the instantaneous fracture process zone for the growing crack). We also compute the Weibull stress using the *maximum* stress that material elements in the process zone have experienced during the entire loading history (see Section 2.2). Figures 13(a–b) compare the evolution of σ_w with J for the shallow notch specimen (growth analysis) using both approaches and for two values of the threshold stress, i.e., $\sigma_{\text{th}} = 0$ and $\sigma_{\text{th}} = 2\sigma_0$. The results confirm our expectation that the Weibull stress values using this alternate treatment for material elements in the partially unloaded region ahead of the advancing tip should be negligibly different. Clearly, it is the elevation of near-tip stress triaxiality and enlargement of the process zone ahead of the crack tip due to stable growth that plays the key role in increasing the total failure probability for the specimen.

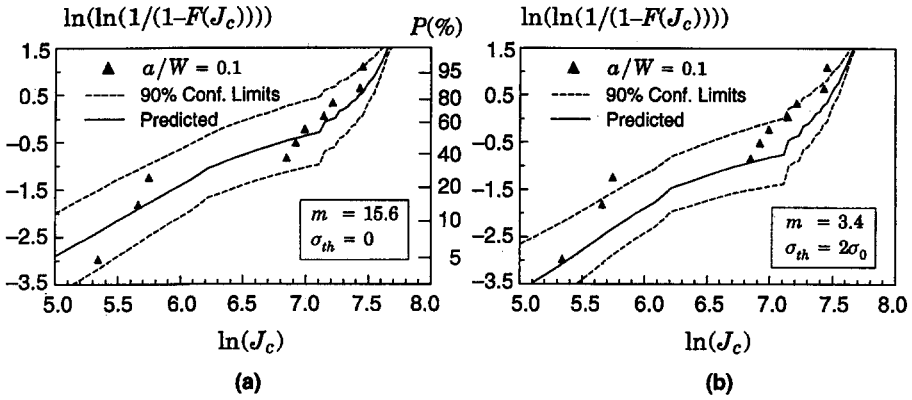

Figure 14. Prediction of the probability distribution for the cleavage fracture toughness data of SE(B) specimens with $a/W = 0.1$. (a) Conventional definition of σ_w with $\sigma_{\text{th}} = 0$. (b) σ_w is calculated upon setting $\sigma_{\text{th}} = 2\sigma_0$.

The Weibull probability plots in Figures 14(a–b) show the predicted distributions of cleavage fracture toughness for the SE(B) specimen with $a/W = 0.1$ using $\sigma_{\text{th}} = 0$ and $\sigma_{\text{th}} = 2\sigma_0$. The solid symbols in the plots indicate the experimental fracture toughness data for those specimens. Values of cumulative probability, F, are obtained by ordering the J_c-values and using $F = (i - 0.5)/N$, where i denotes the rank number and N defines the total number of experimental toughness values. The solid line on each figure represents the *predicted* Weibull distribution generated from the *distribution* (not individual values from tested specimens) of the Weibull stress for the SE(B) specimen with $a/W = 0.5$ using the procedure outlined in Section 3. The dashed lines represent the 90 percent confidence bounds generated from the 90 percent confidence limits for the distribution of the Weibull stress for the SE(B) specimen with $a/W = 0.5$. The predicted distribution for $\sigma_{\text{th}} = 0$ displayed in Figure 13(a) agrees very well with the experimental data; further, all the measured J_c-values lie within the 90 percent confidence bounds. The predicted distribution for $\sigma_{\text{th}} = 2\sigma_0$ shown in Figure 13(b) also agrees reasonably well with the experimental, although providing lower values for the failure probability when compared with Figure 13(a) at the same J; here, only some of the J_c-values lie within the 90 percent confidence bounds.

6. Discussion and concluding remarks

We have presented a probabilistic-based framework to predict the effects of constraint loss and ductile tearing on macroscopic measures of cleavage fracture toughness (J_c, δ_c) applicable for ferritic materials in the ductile-to-brittle transition region. To model the statistics of microcracks and the pronounced effects on scatter of measured J_c-values in the transition region, we employ the Weibull stress σ_w as a near-tip, or *local*, fracture parameter – unstable crack propagation occurs when σ_w attains a critical value. Both constraint loss and ductile tearing affect the evolution of σ_w under increasing applied J in common fracture test specimens. Prior to ductile crack growth in shallow-crack configurations, the Weibull stress strongly reflects the reduced rate at which near-tip stresses increase with applied J due to the constraint loss and the corresponding reduction in the size of the process zone for cleavage fracture. Ductile tearing partially restores the near-tip constraint thereby increasing the cleavage process zone size; the Weibull stress captures these effects of ductile tearing on the near-tip fields.

Applications of this methodology in fracture assessments require mechanical testing, fracture testing and nonlinear finite element analyses for stationary and growing cracks. At the temperature of interest, fracture tests provide:

(1) a population of cleavage toughness values, J_c or equally δ_c, *without* ductile tearing prior to fracture, and

(2) a reference tearing resistance curve for the material.

Mechanical tests provide the true stress-logarithmic strain response for the material. Conventional deep-crack SE(B) specimens usually suffice to generate the J_c data. Shallow-crack SE(B) specimens or other low-constraint configurations, e.g., M(T), SE(T), can sometimes provide an R-curve, although at very low temperatures construction of an R-curve may require the use of J_c-values and measured crack extensions (the procedure followed here in Section 5.2). The non-growth J_c-values enable calibration of the Weibull parameters $\{m, \sigma_u\}$ through stationary crack, finite element analyses of the tested (deep-crack) fracture specimen. Similarly, the R-curve enables calibration of the computational cell parameters $\{D, f_0\}$ using crack-growth, finite element analyses of the specimen configuration tested to generate the R-curve. These micromechanics parameters, $\{m, \sigma_u\}$ for cleavage and $\{D, f_0\}$ for ductile growth, remain fixed for application of the methodology to predict the fracture toughness distributions of other specimen geometries for the material.

The parametric study of small-scale yielding conditions for varying levels of constraint (T-stress) and for a wide range of hardening properties demonstrates the general effects of stress triaxiality and ductile tearing on cleavage fracture through the Weibull stress. Under increasing levels of deformation, cracks imbedded in high constraint fields (positive values of T-stress) maintain high stress levels, whereas low constraint configurations (negative values of T-stress) produce stress fields of much less intensity. The Weibull stress reflects clearly these trends. Crack growth under already high-constraint conditions produces little change in the Weibull stress; crack growth initiated under low constraint conditions elevates the Weibull stress to high-constraint levels – even for low hardening materials. For example, our results show that σ_w continues to increase as the crack advances for a very low hardening material ($n = 20$), which implies a continuing increase in the probability of cleavage fracture.

Our predictions of the probability distribution for cleavage fracture in a high-strength steel based upon the present methodology agree remarkably well with experimental data. Fracture toughness values measured experimentally for a high-constraint geometry that exhibit no prior ductile tearing are effectively 'transferred' to a different geometry having much lower constraint and in which tearing precedes cleavage. The inherent difficulty in predicting the scatter of experimental fracture toughness, as well as constraint and ductile tearing effects, within the scope of conventional procedures appears greatly reduced in the methodology presented here.

While we have not explored an extensive range of crack configurations and loading modes, the relative operational simplicity of the Weibull stress approach, cast in the form of a toughness scaling model, encourages further investigations in direct correlations between laboratory specimens and structural components. We believe a key feature in the success of the present methodology, and of the Dodds–Anderson toughness scaling model as well, lies in the overall similarity of the crack-tip stress fields across the various geometries considered in this and previous studies [11, 60]. The crack-tip stresses in through-crack and surface-crack specimens subjected to uniaxial tension or uniaxial bending all appear remarkably similar except for the amplitude. Moreover, in these configurations ample plastic strains required to nucleate

triggering sites for cleavage develop in the crack-tip region. However, under strong biaxial loading (such as would occur during a pressurized thermal shock (PTS) event in a nuclear reactor) this similarity of stress fields with uniaxially loaded fracture specimens may not hold and, when coupled with the suppressed development of plastic strains, the robustness of our approach remains untested.

Applications of the proposed methodology in the simplified framework of plane-strain models require only modest computational resources – the 1000–1500 element models with extensive ductile crack growth consume at most 4–5 hours of time on desktop workstation. We see no conceptual barrier in applying this approach to fully 3-D computations, including large-scale ductile crack growth. Extensions to address 3-D models of through-crack fracture specimens and surface-crack components require much greater computational resources and very efficient solution procedures. Preliminary efforts along these lines, for example, reveal that detailed models of side-grooved SE(B) specimens containing 8000–10000 elements can be analyzed for 2–3 mm of ductile growth using 800–1000 load steps in 3–4 hours on a Cray C-90 using the WARP3D code. The initial predictions of crack-front profiles and R-curves generated in these computations appear very promising.

Acknowledgements

This investigation was supported by grants principally from the U.S. Nuclear Regulatory Commission, the Naval Surface Warfare Center – Annapolis Detachment (N61533-92-K-0030) and NASA-Ames (NCC2-5022). The authors acknowledge the useful discussions and contributions of Professors M. Toyoda and F. Minami (Osaka University), Dr. Kim Wallin (VTT Finland) and Dr. A. Brückner-Foit (Karlsruhe University). The authors acknowledge Nippon Steel Corporation for making the CTOD test results available. During the final preparation of this paper, the authors became aware of a similar approach described by Xia and Shih [36]. Their work encouraged us to also predict the shallow-crack distributions using a non-zero threshold stress.

References

1. J.W. Hutchinson, Fundamentals of the phenomenological theory of nonlinear fracture mechanics, *Journal of Applied Mechanics* 50 (1983) 1042–1051.
2. R.M. McMeeking and D.M. Parks, On criteria for J-dominance of crack-tip fields in large-scale yielding, *Elastic-Plastic Fracture, ASTM STP 668*, J.D. Landes, J.A. Begley and G.A. Clark (eds.) (1979) 175–194.
3. C.F. Shih and M.D. German, Requirements for a one parameter characterization of crack tip fields by the HRR singularity, *International Journal of Fracture* 17(1) (1981) 27–43.
4. W.A. Sorem, R.H. Dodds and S.T. Rolfe, Effects of crack depth on elastic plastic fracture toughness, *International Journal of Fracture* 47 (1991) 105–126.
5. P.M.S.T. DeCastro, J. Spurrire and P. Hancock, An experimental study of the crack length/specimen width (a/W) ratio dependence of the crack opening displacement (COD) test using small-scale specimens, *Fracture Mechanics, ASTM STP 677*, C.W. Smith (ed.) (1979) 486–497.
6. C. Ruggieri, F. Minami and M. Toyoda, The local approach to the effect of notch depth on fracture toughness in 9^{th} *European Conference on Fracture (ECF9)*, Vol. I, Varna, Bulgaria (1992) 621–626.
7. A.M. Al-Ani and J.W. Hancock, J-dominance of short cracks in tension and bending, *Journal of Mechanics and Physics of Solids* 39 (1991) 23–43.
8. C. Betegon and J.W. Hancock, Two-parameter characterization of elastic-plastic crack tip fields, *Journal of Applied Mechanics* 58 (1991) 104–113.
9. Z.-Z. Du and J.W. Hancock, The effect of non-singular stresses on crack-tip constraint, *Journal of Mechanics and Physics of Solids* 39 (1991) 555–567.
10. D.M. Parks, Advances in characterization of elastic-plastic crack-tip fields, in *Topics in Fracture and Fatigue*, A.S. Argon (ed.), Springer Verlag (1992) 59–98.

11. Y.Y. Wang, On the two-parameter characterization of elastic-plastic crack-front fields in surface-cracked plates, in *Constraint Effects in Fracture, ASTM STP 1171*, Hackett et al. (eds.) (1993) 120–138.
12. N.P. O'Dowd and C.F. Shih, Family of crack-tip fields characterized by a triaxiality parameter: Part I – Structure of fields, *Journal of the Mechanics and Physics of Solids* 39(8) (1991) 989–1015.
13. Ibid, 40 (1992) 939–936.
14. S.B. Batdorf and J.G. Crose, A statistical theory for the fracture of brittle structures subjected to non-uniform polyaxial stresses, *Journal of Applied Mechanics* 41 (1974) 459–464.
15. A.G. Evans, A general approach for the statistical analysis of multiaxial fracture, *Journal of American Ceramic Society* 61 (1978) 302–308.
16. Y. Matsuo, Statistical theory for multiaxial stress states using Weibull's three-parameter function, *Engineering Fracture Mechanics* 14 (1981) 527–538.
17. F.M. Beremin, A local criterion for cleavage fracture of a nuclear pressure vessel steel, *Metallurgical Transactions* 14A (1983) 2277–2287.
18. K. Wallin, T. Saario and K. Torronen, Statistical model for carbide induced brittle fracture in steel, *Metal Science* 18 (1984) 13–16.
19. K. Wallin, The scatter in K_{Ic} results, *Engineering Fracture Mechanics* 19 (1984) 1085–1093.
20. K. Wallin, Statistical aspects of constraint with emphasis on testing and analysis of laboratory specimens in the transition region, in *Constraint Effect in Fracture, ASTM STP 1171*, Hackett et al. (eds.) (1993) 264–288.
21. T. Lin, A.G. Evans and R.O. Ritchie, A statistical model of brittle fracture by transgranular cleavage, *Journal of Mechanics and Physics of Solids* 21 (1986) 263–277.
22. F. Mudry, A local approach to cleavage fracture, *Nuclear Engineering and Design* 105 (1987) 65–76.
23. A. Brückner-Foit, W. Ehl, D. Munz and B. Trolldenier, The size effect of microstructural implications of the weakest link model, *Fatigue and Fracture of Engineering Materials and Structures* 13 (1990) 185–200.
24. T. Thiemeier, A. Brückner-Foit and H. Kolker, Influence of the fracture criterion on the failure prediction of ceramics loaded in biaxial flexure, *Journal of the American Ceramic Society* 74 (1991) 48–52.
25. F. Minami, A. Brückner-Foit, D. Munz and B. Trolldenier, Estimation procedure for the Weibull parameters used in the local approach, *International Journal of Fracture* 54 (1992) 197–210.
26. A. Bakker and R.W.J. Koers, Prediction of cleavage fracture events in the brittle-ductile transition region of a ferritic steel, in *Defect Assessment in Components – Fundamentals and Applications, ESIS/EG9*, Blauel and Schwalbe (eds.) Mechanical Engineering Publications, London (1991) 613–632.
27. R.W.J. Koers, A.H.M. Krom and A. Bakker, Prediction of cleavage fracture in the brittle to ductile transition region of a ferritic steel, in *Constraint Effects in Fracture – Theory and Applications, ASTM STP 1244*, Kirk and Bakker (eds.) (1995) 191–208.
28. C. Ruggieri, F. Minami and M. Toyoda, A statistical approach for fracture of brittle materials based on the chain-of-bundles model, *Journal of Applied Mechanics* 62 (1995) 320–328.
29. R.H. Dodds, T.L. Anderson and M.T. Kirk, A framework to correlate a/W ratio effects on elastic-plastic fracture toughness (J_c), *International Journal of Fracture* 48 (1991) 1–22.
30. T.L. Anderson and R.H. Dodds, Specimen size requirements for fracture toughness testing in the ductile-brittle transition region, *Journal of Testing and Evaluation* 19 (1991) 123–134.
31. A.G. Varias and C.F. Shih, Quasi-static crack advance under a range of constraints – steady state fields based on a characteristic length, *Journal of the Mechanics and Physics of Solids* 41 (1993) 835–861.
32. R.H. Dodds, M. Tang and T.L. Anderson, Effects of prior tearing on cleavage fracture toughness in the transition region, in *Constraint Effects in Fracture, Theory and Application, ASTM STP 1244*, M. Kirk and A. Bakker (eds.) (1993).
33. L. Xia and C.F. Shih, Ductile crack growth – I. A numerical study using computational cells with microstructurally-based length scales, *Journal of the Mechanics and Physics of Solids* 43 (1995) 233–259.
34. L. Xia, C.F. Shih and J.W. Hutchinson, A computational approach to ductile crack growth under large scale yielding conditions, *Journal of the Mechanics and Physics of Solids* 43 (1995) 398–413.
35. L. Xia and C.F. Shih, Ductile crack growth – II. Void nucleation and geometry effects on macroscopic fracture behavior, *Journal of the Mechanics and Physics of Solids*, to appear.
36. L. Xia and C.F. Shih, Ductile crack growth – III. Statistical aspects of cleavage fracture after tearing, *Journal of the Mechanics and Physics of Solids*, to appear.
37. A.L. Gurson, Continuum theory of ductile rupture by void nucleation and growth: Part I – Yield criteria and flow rules for porous ductile media. *Journal of Engineering Materials and Technology* 99, 2–15.
38. V. Tvergaard, Material failure by void growth to coalescence, *Advances in Applied Mechanics* 27 (1990) 83–151.
39. E. Smith, Cleavage fracture in mild steel, *International Journal of Fracture Mechanics* 4 (1968) 131–145.
40. R.O. Ritchie, J.F. Knott and J.R. Rice, On the relationship between critical tensile stress and fracture toughness in mild steel, *Journal of Mechanics and Physics of Solids* 21 (1973) 395–410.

41. W. Feller, *Introduction to Probability Theory and Its Application*, Vol. 1, John Wiley & Sons, Inc. New York (1957).
42. A.M. Freudenthal, Statistical approach to brittle fracture, in *Fracture: An Advanced Treatise. Volume II*, H. Liebowitz (ed.), Academic Press, NY (1968) 592–619.
43. A.G. Evans and T.G. Langdon, Structural ceramics, in *Progress in Materials Science, Volume 21*, B. Chalmers (ed.), Pergamon Press, NY (1976) 171–441.
44. W. Weibull, The phenomenon of rupture in solids, *Ingeniors Vetenskaps Akademien, Handlingar* 153 (1939) 55.
45. C. Ruggieri and R.H. Dodds, WSTRESS: Numerical computation of probabilistic fracture parameters. *Structural Research Series (SRS) 608*, UILU-ENG-95-2013, University of Illinois at Urbana-Champaign, (1996).
46. C. Ruggieri and R.H. Dodds, Numerical computation of probabilistic fracture parameters using WSTRESS, *Engineering Computations*, submitted for publication.
47. C. Ruggieri and R.H. Dodds, Numerical modeling of ductile crack growth for porous plastic materials in 3D using computational cells, *International Journal of Fracture*, to appear.
48. K. Koppenhoefer, A. Gullerud, C. Ruggieri, R. Dodds and B. Healy, WARP3D: Dynamic nonlinear analysis of solids using a preconditioned conjugate gradient software architecture, *Structural Research Series (SRS) 596*, UILU-ENG-94-2017, University of Illinois at Urbana-Champaign (1994).
49. T.J. Hughes, Generalization of selective integration procedures to anisotropic and nonlinear media, *International Journal for Numerical Methods in Engineering* 15 (1980) 1413–1418.
50. B. Moran and C.F. Shih, A general treatment of crack tip contour integrals, *International Journal of Fracture* 35 (1987) 295–310.
51. M.L. Williams, On the stress distribution at the base of a stationary crack, *Journal of Applied Mechanics* 24 (1957) 109–114.
52. O.C. Zienkiewicz, *The Finite Element Method*, 3rd ed., McGraw-Hill, London (1989).
53. M. Toyoda, F. Minami, T. Matsuo, Y. Hagiwara and T. Inoue, Effect of work hardening properties of high strength steels on cleavage/ductile fracture resistance, National Meeting of the Japan Welding Society, 49 (1991) 112–113 (in Japanese).
54. M.T. Kirk and R.H. Dodds, *J* and *CTOD* estimation equations for shallow cracks in single edge notch bend specimens, *Journal of Testing and Evaluation* 24(4) (1993) 228–238.
55. N.R. Mann, R.E. Schafer and N.D. Singpurwalla, *Methods for Statistical Analysis of Reliability and Life Data*, Wiley & Sons, New York (1974).
56. D.R. Thoman, L.J. Bain and C.E. Antle, Inferences on the parameters of the Weibull distribution, *Technometrics* 11 (1969) 445–460.
57. N. Aravas, On the numerical integration of a class of pressure-dependent plasticity models, *International Journal for Numerical Methods in Engineering* 24 (1987) 1395–1416.
58. J.C. Nagtegaal and F.E. Veldpaus, On the implementation of finite strain plasticity equations in a numerical model, in *Numerical Analysis of Forming Processes*, J.F. Pittman, O.C. Ziekiewicz, R.D. Wood and J.M. Alexander (eds.), John Wiley and Sons, New York (1984) 351.
59. B.E. Healy and R.H. Dodds, A large strain plasticity model for implicit finite element analyses, *Computational Mechanics* 9(2) (1992) 95–112.
60. R.H. Dodds, C.F. Shih and T.L. Anderson, Continuum and micro-mechanics treatment of constraint in fracture, *International Journal of Fracture* 64 (1993) 101–133.
61. V. Tvergaard and A. Needleman, Analysis of the cup-cone fracture in a round tensile bar, *Acta Metallurgica* 32 (1984) 157–169.
62. S.G. Larsson and A.J. Carlsson, Influence of non-singular stress terms and specimen geometry on small scale yielding at crack-tips in elastic-plastic materials, *Journal of the Mechanics and Physics of Solids* 21 (1973) 447–473.
63. J.R. Rice, Limitations to the small scale yielding approximation for crack tip plasticity, *Journal of the Mechanics and Physics of Solids* 22 (1974) 17–26.